Title
Neuronal Depolarization Drives Increased Dopamine Synaptic Vesicle Loading via VGLUT

Authors
Aguilar, Jenny I
Dunn, Matthew
Mingote, Susana
et al.

Peer reviewed

Neuronal Depolarization Drives Increased Dopamine Synaptic Vesicle Loading via VGLUT

Jenny I. Aguilar[1,13], **Matthew Dunn**[2,13], **Susana Mingote**[3,4], **Caline S. Karam**[3,4], **Zachary J. Farino**[5], **Mark S. Sonders**[3,4,6], **Se Joon Choi**[3,4], **Anna Grygoruk**[7], **Yuchao Zhang**[3,4], **Carolina Cela**[8], **Ben Jiwon Choi**[9], **Jorge Flores**[10], **Robin J. Freyberg**[5], **Brian D. McCabe**[8], **Eugene V. Mosharov**[3,4,6], **David E. Krantz**[7], **Jonathan A. Javitch**[3,4,11], **David Sulzer**[3,4,6,11], **Dalibor Sames**[2], **Stephen Rayport**[3,4], and **Zachary Freyberg**[5,12,14,*]

[1]Department of Pharmacology, Vanderbilt University, Nashville, TN 37232, USA [2]Department of Chemistry, Columbia University, New York, NY 10027, USA [3]Department of Psychiatry, College of Physicians & Surgeons, Columbia University, New York, NY 10032, USA [4]Division of Molecular Therapeutics, New York State Psychiatric Institute, New York, NY 10032, USA [5]Department of Psychiatry, University of Pittsburgh, Pittsburgh, PA 15213, USA [6]Department of Neurology, College of Physicians & Surgeons, Columbia University, New York, NY 10032, USA [7]Department of Psychiatry and Biobehavioral Sciences and Semel Institute for Neuroscience and Human Behavior, Hatos Center for Neuropharmacology, David Geffen School of Medicine University of California, Los Angeles, CA 90095, USA [8]Brain Mind Institute, EPFL, 1015 Lausanne, Switzerland [9]Center for Motor Neuron Biology and Disease, College of Physicians & Surgeons, Columbia University, New York, NY 10032, USA [10]Department of Biochemistry and Molecular Biophysics, Howard Hughes Medical Institute, College of Physicians & Surgeons, Columbia University, New York, NY 10032, USA [11]Department of Pharmacology, College of Physicians & Surgeons, Columbia University, New York, NY 10032, USA [12]Department of Cell Biology, University of Pittsburgh, Pittsburgh, PA 15213, USA

SUMMARY

The ability of presynaptic dopamine terminals to tune neurotransmitter release to meet the demands of neuronal activity is critical to neurotransmission. Although vesicle content has been assumed to be static, *in vitro* data increasingly suggest that cell activity modulates vesicle content. Here, we use a coordinated genetic, pharmacological, and imaging approach in *Drosophila* to

*Correspondence: freyberg@pitt.edu.
[13]These authors contributed equally
[14]Lead Contact

study the presynaptic machinery responsible for these vesicular processes *in vivo*. We show that cell depolarization increases synaptic vesicle dopamine content prior to release via vesicular hyperacidification. This depolarization-induced hyperacidification is mediated by the vesicular glutamate transporter (VGLUT). Remarkably, both depolarization-induced dopamine vesicle hyperacidification and its dependence on VGLUT2 are seen in ventral midbrain dopamine neurons in the mouse. Together, these data suggest that in response to depolarization, dopamine vesicles utilize a cascade of vesicular transporters to dynamically increase the vesicular pH gradient, thereby increasing dopamine vesicle content.

INTRODUCTION

Depolarization-induced synaptic vesicle (SV) release is dynamic, requiring feedback between the cellular machinery regulating vesicle recruitment, fusion, and recycling. Although initial work on presynaptic neurotransmitter release assumed that SV content was static with neuronal activity (Boyd and Martin, 1956), more recent evidence suggests that vesicles modulate their content to meet the demands of repeated neuronal firing (Pereira and Sulzer, 2012). The ability to tune the amount of neurotransmitter released per vesicle in response to firing adds another level of regulation to synaptic neurotransmission. However, the mechanisms underlying this regulation remain poorly understood, particularly *in vivo*.

SVs utilize the H^+ electrochemical gradient ($\Delta\mu_H^+$) across the vesicle membrane to accumulate and retain neurotransmitter cargo. The vacuolar-type H^+-ATPase (V-ATPase) generates this $\Delta\mu_H^+$ gradient, which is comprised of both a chemical H^+ gradient (ΔpH) and an electrical potential ($\Delta\Psi$), where $\Delta\mu_H^+ = \Delta pH + \Delta\Psi$ (Blakely and Edwards, 2012). Vesicular neurotransmitter transporters, depending on their substrates, rely on ΔpH or $\Delta\Psi$ to differing extents to fill SVs. Manipulating either SV ΔpH, $\Delta\Psi$, or both modifies vesicle content, including glutamate, GABA, and dopamine (DA). While SV loading of glutamate across the vesicular glutamate transporter (VGLUT) is largely $\Delta\Psi$ driven, both the loading and retention of monoamines, including DA, are principally ΔpH driven (Blakely and Edwards, 2012).

Cytoplasmic DA is transported across the SV membrane through the vesicular monoamine transporter (VMAT), which exchanges two luminal H^+ out of the vesicle for every DA molecule that enters. This exchange leads to a transient net intraluminal H^+ loss and establishes dependence on ΔpH for VMAT-mediated DA vesicle loading. Evidence suggests that the interplay between H^+-exchanging vesicle transporters and the V-ATPase dynamically modulates both vesicular ΔpH and quantal size (Hnasko and Edwards, 2012).

Consistent with the idea that vesicular ΔpH is dynamic, *in vitro* stimulation increases secretory vesicle acidification in several secretory cell types, including adrenal chromaffin and thyroid parafollicular cells (Pothos et al., 2002; Tamir et al., 1994). These increases in vesicle ΔpH increase catecholamine content *in vitro* (Pothos et al., 2002). Although such results suggest that depolarization-induced increases in content and intraluminal acidification are part of a unified process, their precise relationship to one another is not known. Moreover, it is unclear whether these phenomena occur in neurons *in vivo*.

We combined genetic, optical, and pharmacological approaches in *Drosophila melanogaster* to study the mechanisms underlying *in vivo* regulation of DA SV pH and content during neuronal stimulation within a viable whole brain. We used a recently developed second-generation fluorescent false neurotransmitter (FFN), FFN206, as a fluorescent DA surrogate (Hu et al., 2013) to visualize the dynamics of SV DA loading and release in presynaptic DA terminals. We also employed dVMAT-pHluorin, a genetically encoded SV pH biosensor (Grygoruk et al., 2014), to observe intraluminal pH changes in response to stimulation. By co-expressing dVMAT-pHluorin with tetanus toxin light chain (TeTxLC), an inhibitor of SV fusion, we studied depolarization-induced pH changes within an intact SV pool, independently of exocytosis. Our findings demonstrate that neuronal depolarization increases DA SV loading in response to increased vesicular acidification prior to exocytic release. Moreover, we show that VGLUT is a critical mediator of this depolarization-induced SV hyperacidification.

We demonstrate that the depolarization-induced effects in *Drosophila* are conserved in mammals. We used a pH-responsive dopaminergic FFN, FFN102 (Rodriguez et al., 2013), to monitor effects of depolarization on SV pH in acute mouse striatal slices. We found that DA vesicles hyperacidify in response to neuronal depolarization in a VGLUT2-dependent manner in mice. Therefore, our findings reveal that these mechanisms are conserved across species. These data introduce a new paradigm for DA/glutamate co-transmission, arguing that vesicular glutamate transport mediates dynamic changes in the SV pH gradient and content during neuronal activity.

RESULTS

Neuronal Depolarization Increases Loading of DA Vesicle Content

We visualized real-time changes in dopaminergic SV content *in vivo* during neuronal depolarization in *Drosophila melanogaster*. We employed a highly fluorescent VMAT substrate, FFN206, to monitor the dynamics of intraluminal DA loading and release in a whole, living, adult fly brain (Figure 1A). FFN206 labels several monoaminergic neuronal populations in wild-type (WT) brain (Freyberg et al., 2016). Therefore, to specifically examine presynaptic DA terminals, we used flies with a complete *Drosophila* VMAT (dVMAT) null genetic background where dVMAT expression was selectively rescued using the DA neuron-specific tyrosine hydroxylase (TH) promoter (termed TH Rescue; Figure 1A).

To measure changes in SV loading and release during neuronal depolarization in FFN206-labeled DA nerve terminals, we super-fused the brain with KCl (40 mM) in the continuous presence of FFN206 (300 nM). The relatively slower cell depolarization kinetics associated with high K^+ application permitted better resolution of depolarization-induced changes in dopaminergic SV content. We focused our analysis on a dense population of presynaptic DA terminals belonging to MB-MV1 neurons. Depolarization led to a distinct, transient ~22% increase in FFN206 fluorescence relative to baseline, suggesting increased loading of vesicle content. This increase was subsequently followed by a decrease in FFN206 fluorescence best fit by a monoexponential decay ($t_{1/2} = 5.2 \pm 0.9$ s), consistent with SV fusion (Figure 1B). To confirm that this transient increase in SV content prior to release was specific to

neuronal depolarization, we examined effects of the lipophilic weak base chloroquine (CQ), which causes FFN destaining through a mechanism different from that of KCl (Freyberg et al., 2016). KCl depolarizes neurons and leads to the exocytic release of SV content into the synaptic space. In contrast, CQ dissipates the vesicular pH and redistributes SV content vesicle out of the lumen into the cytoplasm (Freyberg et al., 2016). CQ (100 μM) application caused FFN206 destaining in DA terminals. However, unlike KCl treatment, CQ treatment did not cause increased FFN206 loading prior to destaining (Figure 1B).

DA Vesicles Hyperacidify in Response to Neuronal Depolarization

Given the role of pH in driving vesicular loading and retention of monoamines, we hypothesized that depolarization-induced increases in DA SV loading were due to an increase in vesicular pH. To test this, we optically monitored real-time changes in intraluminal pH in dopaminergic SVs within our whole, adult fly brain preparation using dVMAT-pHluorin. We selectively expressed dVMAT-pHluorin in presynaptic DA neurons using the TH promoter and focused our analysis on the terminals within MB-MV1 (Figure 1C), where we conducted our FFN206 recordings. This TH-driven dVMAT-pHluorin expression closely resembled the distribution of FFN206 labeling in TH Rescue brains, consistent with selective labeling of DA terminals (Figure 1C).

We found that high K^+ stimulation (40 mM KCl) produced a rapid increase in dVMAT-pHluorin fluorescence followed by a slower decline in signal in presynaptic DA terminals (Figure 1D). This pattern is characteristic of rapid exocytic SV fusion, which moves the pHluorin sensor from the acidic vesicle lumen to the neutral extracellular space. Significantly, we found a brief ~15% decrease in dVMAT-pHluorin fluorescence prior to exocytic fusion, representing increased intraluminal acidification relative to the pre-application baseline. To rule out potential effects of sustained KCl application, we acutely delivered KCl by focal pressure ejection (Figure S1). The change in dVMAT-pHluorin fluorescence following pressure ejection was similar to that following bath application, albeit with considerably faster onset due to more rapid drug delivery (Figure S1). Moreover, the timing of maximal vesicular acidification relative to onset of KCl treatment (22.4 ± 8.6 s) overlapped with maximal vesicular FFN filling (31.8 ± 12.9 s; p > 0.05), suggesting that increases in depolarization-induced SV hyperacidification and DA loading occur concomitantly. In summary, we show that stimulation of presynaptic DA terminals increases vesicular DA loading and intraluminal hyperacidification prior to release.

Inhibition of Exocytic Fusion Unmasks Significant Depolarization-Induced SV Hyperacidification

It is likely that the changes in dVMAT-pHluorin fluorescence during stimulation represented the *net* pH changes in two distinct SV populations ($F_{total} = F_{fusing} + F_{intact}$): (1) vesicles engaging in active exocytic fusion that increase the dVMAT-pHluorin signal by shifting the sensor from the acidic lumen to the neutral extracellular environment (F_{fusing}) and (2) intact, unfused vesicles exhibiting increased SV acidification that diminish the dVMAT-pHluorin signal (F_{intact}). To isolate the F_{intact} signal, we co-expressed genetically encoded TeTxLC to block vesicular exocytic fusion with dVMAT-pHluorin inpresynaptic DA

neurons. This allowed us to measure the effects of neuronal stimulation on the pH of intact SVs without the obscuring pH changes of concomitant exocytic vesicle fusion.

TeTxLC-expressing flies did not exhibit the sharp rise in dVMAT-pHluorin fluorescence intensity in DA terminals induced by KCl stimulation that we observed in non-TeTxLC-expressing control flies (Figures 2A and 2B, highlighted in yellow). Instead, in the absence of vesicle fusion, KCl stimulation caused a 22.9% ± 2.5% decrease in dVMAT-pHluorin fluorescence relative to the unstimulated baseline, suggesting significant hyperacidification (Figures 2A and 2B). The magnitude of this SV hyperacidification was greater than in the DA terminals of control flies, where exocytic vesicle fusion was not blocked (14.7% ± 1.9%, p = 0.037; Figure 2C, left). Interestingly, the kinetics of this hyperacidification was unchanged in the absence of exocytic vesicle fusion compared to the control (p > 0.05; Figure 2C, right). Moreover, brains superfused with vehicle alone exhibited no change in dVMAT-pHluorin fluorescence over time, making it unlikely that photobleaching of the dVMAT-pHluorin signal contributed to depolarization-induced decreases in fluorescence (Figure 2B).

We examined the temporal relationship between neuronal depolarization and DA vesicle hyperacidification by correlating the kinetics of KCl-induced SV hyperacidification with that of DA neuron depolarization using the genetically encoded plasma membrane-localized voltage sensor, ArcLight (Cao et al., 2013) (co-expressed with TeTxLC in the same terminals). We found that the timing of depolarization (46.1 ± 6.7 s), as indicated by the maximal decline in ArcLight fluorescence, preceded vesicular hyperacidification in DA terminals (71.9 ± 5.9 s, p = 0.03; Figure 2D), suggesting that changes in vesicular pH are depolarization dependent.

Chloride Channels Do Not Mediate Depolarization-Induced SV Hyperacidification in DA Nerve Terminals

Earlier work demonstrated that anion uptake into the vesicle lumen drives further SV acidification by diminishing vesicular Ψ and subsequently increasing pH (Hnasko and Edwards, 2012). These studies, conducted primarily *in vitro*, suggested an important role for the physiological anion chloride (Cl^-) in mediating acidification of intracellular organelles, including SVs. Therefore, we investigated possible roles for Cl^- and Cl^- transport in mediating depolarization-induced SV hyperacidification. Potential candidates in mediating Cl^--dependent intraluminal pH changes include voltage-gated Cl^- channels (ClCs), which act as Cl^-:H^+ antiporters and have been associated with regulation of vesicle pH and quantal size (Takamori, 2016a).

To examine the contribution of ClCs to depolarization-induced SV hyperacidification in DA terminals, we used the ClC inhibitor 5-Nitro-2-(3-phenylpropylamino)benzoic acid (NPPB) (Figure 3A). Acute NPPB pre-treatment altered neither the magnitude nor the kinetics ($t_{1/2}$) of KCl-induced hyperacidification compared to control brains pre-treated with vehicle (p > 0.05; Figures 3A and 3B). These data suggest that acute ClC inhibition does not directly modify pH changes observed in DA SVs in response to depolarization.

Since there are multiple routes for vesicular Cl^- flux besides ClCs (Eriksen et al., 2016), we examined Cl^-'s potential contribution to depolarization-induced DA vesicle hyperacidification more generally. We halved the extracellular Cl^- present during high K^+ neuronal stimulation by isosmotically substituting Cl^- with gluconate (20 mM Cl^-; Figure 3C). Decreasing extracellular Cl^- neither altered the magnitude nor the half-life ($t_{1/2}$) of SV hyperacidification in DA terminals compared to the unsubstituted control (40 mM Cl^-, $p > 0.05$; Figure 3C). Interestingly, this lower Cl^- concentration significantly delayed the time to maximal acidification from onset of KCl stimulation compared to the control ($p = 0.01$). Our results suggest that limiting Cl^- currents by acute ClC inhibition or diminishing the availability of extracellular Cl^- does not significantly alter the magnitude of depolarization-induced SV hyperacidification in DA terminals. Therefore, we examined whether an alternative anion, such as glutamate, mediates depolarization-induced changes in SV Ψ.

dVGLUT and dVMAT Co-localize in *Drosophila* Presynaptic DA Nerve Terminals

It has been established that mammalian DA neurons are capable of glutamate co-transmission (Hnasko and Edwards, 2012). In addition to its function as a neurotransmitter, glutamate has also been implicated in modulating DA vesicle pH (Hnasko et al., 2010). However, whether this was also the case in *Drosophila* was unknown. To examine whether glutamate was involved in depolarization-induced SV hyperacidification in fly DA terminals, we first determined whether SV glutamate transporters, which transport cytoplasmic glutamate into the SV lumen, are present in adult fly DA terminals. In contrast to mammals, which express three VGLUT isoforms with distinct developmental patterns, localization, and function, flies express a single VGLUT isoform, dVGLUT. We first co-expressed two spectrally separable fluorescent tags driven by dVGLUT-LexA (mCherry) and TH-GAL4 (mCD8::GFP) expression drivers in a WT background to examine potential co-localization of dVGLUT(+) and TH(+) neurons (Figure 4). dVGLUT labeling was detected throughout most of the brain neuropil, while TH(+) neuronal labeling was more circumscribed. We found that dVGLUT- and TH promoter-driven fluorescent tags co-localized in the MB-MV1 region, particularly within DA nerve terminal active zones labeled by Bruchpilot, a synaptic active zone marker (using the nc82 antibody; Figures 4A and 4B; Figure S2). We validated these data by determining whether endogenous dVGLUT co-localized to presynaptic DA nerve terminals using an anti-dVGLUT antibody (Daniels et al., 2004) in fly brains expressing TH promoter-driven dVMAT-pHluorin (Figure S3). To identify areas of overlap between dVMAT(+) and dVGLUT(+) antibody labeling unambiguously, we focused our attention on cells and their processes that clearly expressed dVMAT-pHluorin and were also spatially separate from other dVGLUT labeling. Among individual DA terminals, we found clear co-localization of dVGLUT and dVMAT-pHluorin fluorescent signals, where $4.0\% \pm 1.3\%$ of dVMAT(+) terminals were also VGLUT(+). Significantly, within dense clusters of DA terminals, including MB-MV1, we observed $21.5\% \pm 0.2\%$ signal overlap. We also observed similar co-localization of dVMAT and dVGLUT in discrete clusters within DA neuron cell bodies (Figure S3).

dVGLUT Drives Depolarization-Induced SV Hyperacidification in DA Nerve Terminals

Based on our co-localization between dVGLUT and dVMAT and evidence of VGLUT2's modulatory role in mammalian DA neuron SV pH (Hnasko et al., 2010), we reasoned that

glutamate transport across dVGLUT into the SV lumen might provide the anion flux necessary to potentiate depolarization-induced changes in pH in presynaptic DA terminals (Figure 5A). To test this, we selectively knocked down dVGLUT expression in presynaptic DA terminals via TH-GAL4-driven dVGLUT RNAi. We confirmed dVGLUT knockdown by qRT-PCR; dVGLUT RNAi reduced dVGLUT expression to 25.5% ± 5.0% of control levels (p = 0.0002; Figure S4A; Table S1). We validated further the effects of dVGLUT RNAi functionally. Consistent with evidence that presynaptic dVGLUT mediates miniature neurotransmission at the neuromuscular junction (NMJ) (Choi et al., 2014), expression of dVGLUT RNAi in presynaptic glutamatergic larval motor neurons significantly inhibited the frequency of miniature excitatory postsynaptic potentials (mEPSPs) (p < 0.01; Figure S4B). The amplitude of the few remaining mEPSPs was not altered (p > 0.05; Figure S4C), suggesting that the effects of dVGLUT RNAi-mediated knockdown were primarily presynaptic.

Reducing dVGLUT expression in presynaptic DA neurons significantly attenuated the magnitude of depolarization-induced SV hyperacidification in DA terminals ($-F/F_i = 15.9\% \pm 0.7\%$) compared to the TH-GAL4 control ($-F/F_i = 26.4\% \pm 2.7\%$, p = 0.04; termed non-RNAi control) (Figure 5A); there was no significant difference between mCherry RNAi and non-RNAi controls (p > 0.05; Figure 5C). dVGLUT knockdown did not change the kinetics or timing of hyperacidification compared to non-RNAi and mCherry RNAi controls (p > 0.05; Figure 5D). In parallel, acute dVGLUT inhibition with the VGLUT-specific inhibitor Rose Bengal (RB) attenuated depolarization-induced increases in DA vesicle loading (Figure S5). These data provide independent confirmation of dVGLUT's role in depolarization-induced increases in SV acidification and loading.

In light of evidence that VGLUT can transport both glutamate and Cl^- into SVs (Preobraschenski et al., 2014), we examined the potential contribution of Cl^- to dVGLUT-mediated SV hyperacidification during stimulation. We halved the extracellular Cl^- (20 mM Cl^-) during high K^+ stimulation by isosmotic gluconate substitution in brains, where DA terminal dVGLUT expression was already knocked down (Figure 5B). Diminished extracellular Cl^- did not alter the magnitude of depolarization-induced SV hyperacidification in the dVGLUT knockdown background ($-F/F_i = 15.9\% \pm 0.7\%$) compared to high K^+ stimulation with 40 mM Cl^- ($-F/F_i = 12.4\% \pm 2.9\%$; p > 0.05) (Figure 5C). However, it significantly delayed the kinetics ($t_{1/2}$) and time to reach maximal intraluminal acidification compared to the unsubstituted control in presynaptic DA terminals (Figure 5D). Thus, dVGLUT expression in DA neurons is a key mediator of depolarization-induced changes in SV pH. Although transport of Cl^- across dVGLUT does not modify the magnitude of depolarization-induced increases in SV pH, our data suggest that Cl^- may modulate the timing of this event.

Since reducing dVGLUT expression significantly diminished depolarization-induced SV hyperacidification, we examined whether dVGLUT overexpression would increase the magnitude of this vesicular hyperacidification in DA terminals. We used the TH promoter to drive overexpression of dVGLUT selectively in presynaptic DA neurons (Figure S6). dVGLUT overexpression significantly enhanced depolarization-induced SV hyperacidification compared to controls expressing WT levels of the transporter (82.4%

increase relative to the control; p = 0.002) (Figures S6A and S6B). In contrast, dVGLUT overexpression did not significantly alter the kinetics ($t_{1/2}$) to reach maximal acidification compared to the control (p >0.05; Figure S6B). Our results therefore show that dVGLUT bidirectionally mediates depolarization-induced SV hyperacidification in DA nerve terminals.

dVGLUT Modulates the DA-Mediated Locomotor Response to Amphetamine

We examined whether changes in dVGLUT expression in DA neurons modify DA-dependent behaviors in *Drosophila*, specifically basal locomotion and amphetamine (AMPH)-induced hyperlocomotion (Pizzo et al., 2013). DA neuron-selective dVGLUT knockdown diminished basal locomotion compared to control flies (p = 0.038; Figure 6A). dVGLUT knockdown in DA neurons also lowered rates of activity following treatment with AMPH (10 mM) compared to control flies (p < 0.0001; Figure 5E). Conversely, dVGLUT overexpression in these neurons increased basal locomotion (p = 0.018; Figure 5F), consistent with the bidirectional pH effects above (Figure 5; Figure S6). dVGLUT over-expression also rendered flies more sensitive to AMPH's effects on locomotion. While WT flies typically responded to 10 mM AMPH, flies with TH-driven dVGLUT overexpression exhibited robust AMPH-induced hyperlocomotion in response to 5 mM AMPH—a concentration otherwise insufficient to elicit hyperlocomotion in control flies (p > 0.05; Figure 5F). Overall, these results validate a modulatory role for dVGLUT in DA neurons *in vivo*.

NHEs Mediate Depolarization-Induced Changes in SV pH and Quantal Content in DA Nerve Terminals

We examined the mechanisms driving glutamate uptake across dVGLUT into DA vesicles in response to cell depolarization. Depolarization increases the intracellular concentration of cations, including Na^+ (Pothos et al., 2002). In glutamate-containing SVs, ($Na^+$and K^+)/H^+exchangers (NHEs) utilize this cation influx to mediate changes in both pH and vesicle content by increasing Ψ (Goh et al., 2011). Since Ψ is the primary driving force for vesicular glutamate uptake, NHE activity leads to corresponding increases in vesicular glutamate content (Goh et al., 2011). Therefore, we asked whether NHE-mediated cation (Na^+ and K^+)/H^+ exchange functions similarly in DA SVs during depolarization to promote glutamate transport across dVGLUT and increase pH in presynaptic DA terminals (Figure 6A). In DA terminals co-expressing TeTxLC and dVMAT-pHluorin, brief pre-treatment with NHE inhibitor 5-(N-ethyl-N-isopropyl) amiloride (EIPA; 50 μM) significantly diminished the magnitude of SV hyperacidification following KCl stimulation (− F/F$_i$ = 16.6% ± 1.3%) compared to the vehicle condition (− F/F$_i$ = 30.8% ± 4.0%; p = 0.02) (Figures 6A and 6B, left). EIPA inhibition also significantly slowed the kinetics (p = 0.004) and timing (p = 0.03) of depolarization-induced hyperacidification compared to the non-EIPA pre-treated condition (Figure 6B, middle and right). Similarly, in the absence of TeTxLC's inhibition of SV fusion, EIPA treatment reduced depolarization-induced SV hyperacidification immediately preceding SV exocytosis in DA terminals (AUC = 1.6 ± 0.7) compared to non-treated controls (AUC = 2.8 ± 0.2; p < 0.05, Figure 6C) but did not significantly affect the timing of subsequent vesicle exocytosis (data not shown, p > 0.05).

Since acute NHE inhibition attenuated depolarization-induced increases in DA vesicle pH, we asked whether EIPA inhibition also diminished the corresponding increases in vesicle content during KCl stimulation, as described above (see Figure 1A). Using FFN206, we found no additional vesicular loading following EIPA pre-treatment in DA terminals of TH Rescue brains compared to the non-treated controls (Figure 6D). Moreover, EIPA significantly slowed the kinetics of FFN206 destaining compared to non-EIPA treated controls (p = 0.005; Figure 6D). Our findings suggest that cell depolarization is coupled to changes in both SV pH and vesicle content in DA terminals via NHEs.

Depolarization-Induced SV Hyperacidification Occurs in Mammalian DA Nerve Terminals

We asked whether depolarization-induced SV hyperacidification similarly occurred in mammalian DA nerve terminals. We used FFN102, a fluorescent substrate of both the mammalian dopamine transporter (DAT) and VMAT2 (Rodriguez et al., 2013), to report real-time changes in SV pH in acute mouse ventral striatal brain slices. Unlike FFN206, which only acts as a reporter of monoaminergic SV content (Hu et al., 2013), FFN102's photophysical properties also render it a sensitive ratiometric reporter of pH (pK_a = 6.2). The probe's protonated and deprotonated forms exhibit distinct, pH-dependent excitation maxima and fluorescence emission intensities (Figure S7A). The fluorescence ratio generated from the respective excitation wavelengths of the protonated and deprotonated forms of FFN102 permits calculation of the relative intraluminal pH changes within FFN102-labeled nerve terminals (Rodriguez et al., 2013).

We observed an ~6-fold increase in striatal SV acidification in response to high K^+ stimulation compared to vehicle treatment (p = 0.03), as indicated by the significant shift in the equilibrium from FFN102's deprotonated toward protonated forms (Figures 7A and 7B; Figure S7). We also examined the role of VGLUT2 in depolarization-induced DA SV hyperacidification since, of the three mammalian VGLUT isoforms, VGLUT2 is expressed in terminals of a subset of ventral tegmental area (VTA) DA neurons projecting to the nucleus accumbens (NAc) (Hnasko et al., 2010). VGLUT2 expression in SVs of these DA neurons facilitates DA vesicular filling in isolated vesicle preparations (Hnasko et al., 2010). To examine VGLUT2's role in depolarization-induced increases in SV pH, we generated a VGLUT2 conditional knockout (cKO) mouse. VGLUT2 expression was selectively disrupted in VTA neurons and their NAc projections via injection of AAV-driven mCherry-labeled Cre recombinase (AAV-DJ EF1a-mCherry-cre) in the VTA of adult VGLUT2[flox/flox] mice (Tong et al., 2007); AAV-driven mCherry alone (AAV-DJ-EF1a-mCherry) served as a control (Figure 7C). The majority of TH-labeled pre-synaptic DA neurons in the VTA demonstrated Cre immunostaining (Figure S8A), although a small number of VTA neurons were either Cre(+)/TH(−) or Cre(−)/TH(+) since the Cre expression was not selective to DA neurons. In contrast, there was no Cre immunostaining in the VTA of mCherry alone-injected mice. Furthermore, we found almost complete co-localization of TH-and mCherry immunoreactivity in the primarily dopaminergic nerve terminals of the NAc, further confirming successful transduction of both AAV-driven mCherry-Cre and the mCherry control (Figure S8B). Imaging FFN102-labeled nerve terminals in the NAc core from these VGLUT2 cKO mice demonstrated a significant reduction in KCl-stimulated SV hyperacidification compared with the mCherry control (p = 0.03; Figure 7D). These data

suggest that VGLUT2 mediates the increases in vesicular pH during stimulation in mammalian DA nerve terminals. Moreover, the subsequent increase in FFN102 fluorescence intensity in both the VGLUT2 cKO and control slices indicated that vesicular exocytosis was likely unaffected (Figure 7D).

We evaluated the dependence of these VGLUT2 effects on NHE activity (Figure 7E). Acute NHE inhibition by EIPA (25 μM) completely attenuated depolarization-induced SV hyperacidification prior to exocytic SV release compared to the non-EIPA treated controls (p = 0.03; Figure 7F). NHE inhibition also led to an earlier onset of exocytic SV release as indicated by the sustained rise in FFN102 fluorescence intensity (Figure 7F).

We validated the above results by measuring electrical stimulation-evoked DA release via fast-scan cyclic voltammetry (FSCV) in the presence or absence of EIPA. Given that our earlier data were acquired during periods of extended high K^+ stimulation, we determined whether NHE inhibition is more likely to produce changes in evoked DA release in response to sustained (trains of 20 pulses delivered at 20 Hz) versus brief (single pulse) electrical stimulation (Figure 7G). EIPA pre-treatment had no significant effect on evoked DA release following single pulse (SP) stimulation compared to vehicle controls (p > 0.05; Figure 7H). In contrast, following three trains of stimulation, EIPA pre-treatment significantly diminished evoked DA release compared to vehicle (p = 0.004; Figure 7I). Interestingly, in the control slices treated with vehicle alone, we observed a significant increase in evoked DA release following repeated trains of stimulation (train 1 versus 3; p = 0.018).

Overall, our results suggest that depolarization-induced SV hyperacidification in presynaptic DA terminals is conserved between flies and mammals as are the intrinsic cellular and vesicular mechanisms responsible for mediating these effects.

DISCUSSION

Here, we show—for the first time—regulation of vesicular DA content in response to depolarization *in vivo*. We demonstrate that increases in DA SV content during periods of neuronal activity require the interplay of several transporters, including VGLUT, to enhance pH and thus drive DA vesicle filling through VMAT. Specifically, depolarization produces a concomitant increase in DA SV content and acidification prior to exocytic release. Importantly, our results suggest that DA vesicle pH is dynamic, changing in response to cellular states. Cell stimulation has been shown to modulate the concentrations of intracellular ions, including H^+, in the cytosol (Rossano et al., 2017). Likewise, the intraluminal pH of vesicular compartments, including secretory granules, changes in response to stimulation (Pothos et al., 2002). Nevertheless, the mechanisms underlying these depolarization-induced changes in SV pH have been unclear.

Cl^- is an abundant cellular anion and acts as a modulator of pH in several cell organelles, including SVs (Takamori, 2016b). In mammalian cells, the vesicular Cl^- channel ClC3 has also been implicated in mediating Cl^--induced SV acidification (Takamori, 2016a). We showed that acute inhibition of ClCs does not attenuate the magnitude of DA SV hyperacidification following stimulation, suggesting that ClCs are not the principal

determinant of this change in pH. Most studies examining ClC3's role in SV acidification have been conducted in glutamatergic systems (Takamori, 2016a). However, far less is known about the contribution of ClCs to DA SV acidification and vesicle content. Our data are consistent with *in vitro* measurements in purified vesicle preparations, demonstrating no change in DA uptake in the absence of ClC3 expression (Takamori, 2016a). These results do not rule out the possibility that Cl⁻ influx drives hyperacidification since there are alternative routes of Cl⁻ entry into the vesicle lumen (Takamori, 2016a). To address further the role of Cl⁻ influx in mediating DA SV pH, we decreased extracellular Cl⁻ by isosmotic gluconate substitution. This effectively decreased the concentration gradient driving Cl⁻ entry into the vesicle lumen through ClCs and/or additional routes. Diminishing the driving force for Cl⁻ entry using this approach did not attenuate the magnitude of depolarization-induced hyperacidification. However, Cl⁻ substitution significantly delayed SV hyperacidification in response to stimulation. These data suggest that although Cl⁻ does not itself drive hyperacidification in DA SVs, it may modulate the timing of this phenomenon.

In the absence of experimental data demonstrating that Cl⁻ mediates the magnitude of depolarization-induced DA SV hyperacidification, we hypothesized that another counterion may be driving this process. We speculated that glutamate may be this alternate counterion given: (1) increasing evidence demonstrating that specific neuronal populations release both monoamines and glutamate in mammals (Hnasko and Edwards, 2012) and (2) findings in reconstituted vesicle systems showing that VGLUT is sufficient to increase pH (Schenck et al., 2009). Specifically, we hypothesized that glutamate transport through VGLUT is necessary to decrease Ψ and subsequently drive depolarization-induced hyperacidification. Though several studies have shown co-localization between VMAT2 and VGLUT2 in mammalian DA neurons (Hnasko et al., 2010; Zhang et al., 2015), it was unknown whether this was also the case in *Drosophila*. We found that dVGLUT and dVMAT co-localized in limited subpopulations of presynaptic DA terminals in *Drosophila* adult central brain, including MB-MV1. This suggests region-specific enrichment of dVGLUT co-localization in fly DA terminals, analogous to increased VGLUT2 co-localization in DA terminals of the nucleus accumbens in mammals. Our percentages of co-localization fit well within the values reported in rodent nucleus accumbens ranging from 2% to 25% (Dal Bo et al., 2008). This suggests that co-localization between these two transporters is conserved across species.

To date, the anatomical and functional relationships between VGLUT and VMAT remain controversial. Neuroanatomical evidence from rodent VTA DA neurons shows that subpopulations of their projections can release both DA and glutamate (Barker et al., 2016; Chuhma et al., 2009). Moreover, VGLUT2 and VMAT2 are co-expressed in these same neurons (Hnasko et al., 2010; Morales and Root, 2014). Currently, however, there is no ultrastructural evidence demonstrating co-localization of these transporters to the same vesicles. VGLUT2 and VMAT2 have been shown to segregate in discrete subpopulations of vesicles within the same axons of mesoaccumbens fibers (Barker et al., 2016; Zhang et al., 2015). Though these ultrastructural immunolabeling studies examined fields in great detail, the areas sampled to determine transporter localization in these earlier studies are limited. Therefore, we cannot exclude the possibility that earlier ultrastructural studies may have missed populations of SVs with lower levels of VGLUT2/VMAT2 co-expression and co-

localization. Indeed, as little as a single vesicular glutamate transporter is sufficient to fill a SV (Daniels et al., 2006). Our data are consistent with earlier biochemical evidence showing that VGLUT2(+) SVs isolated from rat ventral striatum also expressed VMAT2 and vice versa by reciprocal immunoprecipitation (Hnasko et al., 2010). Moreover, previous electrophysiological evidence showed that: (1) VGLUT2 knockdown in DA neurons decreases evoked DA release as measured by *ex vivo* fast-scan cyclic voltammetry and (2) glutamate stimulates monoamine uptake in a subpopulation of DA SVs (Hnasko et al., 2010). Thus, although it remains possible that VGLUT2 may regulate DA vesicle content indirectly while localized to distinct non-VMAT(+) SV population(s), a parsimonious explanation is that VMAT2 and VGLUT2 are co-expressed in vesicles in varying amounts within DA terminals.

To study further VGLUT's role in DA neurotransmission *in vivo*, we used AMPH to stimulate vesicular DA release independent of depolarization. AMPH-stimulated hyperlocomotion increased with dVGLUT overexpression in presynaptic DA neurons, consistent with the idea that glutamate enhances vesicular monoamine uptake (Hnasko et al., 2010). Moreover, overexpression of dVGLUT in DA neurons increased sensitivity to AMPH action *in vivo*. Conversely, DA neuron-selective RNAi-mediated knockdown of dVGLUT decreased both basal locomotion and AMPH-induced hyperlocomotion, suggesting that DA vesicle content is diminished in these neurons. Similarly, earlier work in mice showed that VGLUT2 knockdown in DA neurons reduced loco-motor response to AMPH or cocaine (Birgner et al., 2010; Hnasko et al., 2010). While cocaine and AMPH work through distinct mechanisms, both induce hyperlocomotion by causing increases in extracellular DA (Sulzer, 2011). Consequently, decreased locomotion in response to either drug suggests reduced vesicular DA stores. Taken together, our behavioral data in *Drosophila* validate the significance of VGLUT in mediating vesicular DA content.

Consistent with the importance of dVGLUT in DA-mediated behavior, we found that decreasing the expression of dVGLUT in presynaptic DA terminals significantly decreased depolarization-induced hyperacidification in whole, living brain, while over-expression of dVGLUT enhanced this effect. These data suggest that glutamate, as an anion, dissipates Ψ and thus promotes an increase in pH across the DA SV membrane. Our results therefore demonstrate that DA neurons across species take advantage of this VGLUT-dependent mechanism to augment pH and increase DA vesicle content during depolarization. We also investigated whether VGLUT-mediated Cl⁻ transport contributed to depolarization-induced hyperacidification. Although dVGLUT knockdown diminished hyperacidification, limiting Cl⁻ within this genetic background did not modify the SV pH gradient further. Interestingly, Cl⁻ substitution with gluconate, a VGLUT-impermeant anion, significantly delayed the time course of hyperacidification. This delay may be explained by previous studies showing that Cl⁻ modulates VGLUT activity, where decreasing external Cl⁻ concentrations significantly reduces VGLUT2-associated currents (Eriksen et al., 2016). Thus, it is possible that under low Cl⁻ conditions, VGLUT-dependent hyperacidification is delayed because glutamate transport by VGLUT is slowed.

We found that acute inhibition of NHE activity attenuated SV hyperacidification and eliminated the increase in DA loading in SVs in response to depolarization. Although our

experimental data in both flies and mice suggest that NHEs mediate hyperacidification (increase in pH), these transporters also diminish pH through their function as H^+ antiporters. To explain this potential discrepancy, we propose that NHE-mediated cation/H^+ exchange promotes the conversion of vesicular pH to Ψ, as previously shown in glutamate-containing SVs (Goh et al., 2011). One possibility is that SVs maintain a constant electrochemical gradient (μ_H^+) across the vesicle membrane in response to NHE activity. Thus, NHE-mediated decreases in pH cause a corresponding increase in vesicular membrane potential (Ψ), according to the equation $\mu_H^+ = $ pH $ + \Psi$. This rise in Ψ increases the driving force for VGLUT-mediated glutamate uptake. VGLUT functions as a substrate:H^+ antiporter, exchanging one H^+ for every glutamate/Cl^- transported into the vesicle lumen (Blakely and Edwards, 2012). Consequently, the rise in intraluminal negative charge (which diminishes Ψ), and loss of H^+ (which diminishes pH), leads to an overall decrease in μ_H^+. We suggest that, to overcome this drop in μ_H^+, the V-ATPase pumps additional H^+ into the vesicle lumen. This leads to an overshoot in intraluminal H^+, which produces hyperacidification during depolarization, consistent with glutamate's ability to increase DA vesicle acidification more generally (Hnasko et al., 2010). Finally, the rise in pH increases the driving force for VMAT-dependent loading of DA into SVs.

Alternatively, it is possible that μ_H^+ does not remain constant in response to NHE activity during depolarization. Rather, NHEs may contribute to a decrease in μ_H^+ by diminishing pH without significantly changing Ψ since these transporters carry out an electroneutral (Na^+ or K^+)/H^+ exchange (Goh et al., 2011). In this scenario, VGLUT further decreases μ_H^+ as above, ultimately leading to the observed increases in intraluminal pH and SV content through the combined actions of the V-ATPase and VMAT. Ultimately, both scenarios lead us to speculate that NHE-mediated cation exchange couples depolarization-induced cation influx through the plasma and SV membranes with DA SV hyperacidification. Nevertheless, the precise mechanisms by which NHEs mediate these changes in intraluminal pH remain a subject of open discussion, requiring further clarification.

Significantly, we found that depolarization-induced hyperacidification in DA SVs is phylogenetically conserved in mammals. As in *Drosophila*, our *ex vivo* data in ventral striatal slices show that the underlying mechanisms driving this increase in pH require the activities of both VGLUT2 and NHEs. cKO of VGLUT2 expression and pharmacological inhibition of NHE activity both attenuated depolarization-induced changes in pH. Our findings provide a mechanism for earlier observations made by Hnasko and colleagues, who showed that VGLUT2 KO mice have decreased evoked DA release in the ventral striatum (Hnasko et al., 2010).

In addition to our use of elevated extracellular K^+, we employed electrical stimulation to achieve neuronal depolarization under more physiologic circumstances. Although the physiological firing rates of DA neurons in *Drosophila* central brain are poorly characterized, the activity of DA neurons in rodents has been studied extensively. VTA neurons in mice tonically fire at 1–9 Hz and may exhibit periods of burst firing at ~20 Hz (Grace and Bunney, 1984). We paired electrical stimulation with FSCV in mouse NAc to detect effects of acute NHE inhibition on evoked DA release. NHE inhibition decreased

evoked DA release following repeated trains of stimulation but had no significant effect in response to SP stimulation. Conversely, sustained stimulation enhanced evoked DA release in the control condition. These data suggest that DA neurons meet the increased demands of sustained firing with increased DA levels in an NHE-dependent manner through the mechanism outlined below.

Here, we propose the following model for increases in DA SV acidification and content in response to neuronal stimulation (Figure 8): (1) DA neuron depolarization causes an influx of cations, including Na^+, into the cytoplasm. (2) Monovalent cation:H^+ exchange via vesicular NHEs produces a transient drop in intraluminal H^+ (pH). To maintain a constant μ_{H^+}, Ψ rises. (3) This increase in Ψ provides the driving force for increased glutamate transport across VGLUT into the vesicle lumen. (4) The resulting buildup of intraluminal negative charge increases the vesicular proton-motive force, causing the V-ATPase to pump more H^+ into the vesicle lumen. (5) The rise in pH increases the driving force for VMAT-dependent loading of DA into SVs. This model suggests that several transporters, including NHEs, VGLUT, VMAT, as well as the V-ATPase, work in concert to facilitate dynamic changes in DA vesicle pH and content in response to neuronal stimulation.

Consistent with this model, our earlier work showed that DAT and VMAT function in tandem to concentrate DA first in the cytoplasm and ultimately into SVs, respectively (Freyberg et al., 2016). The experimental system used here preserves the cellular function and localization of the presynaptic machinery, which allowed us to resolve the individual contributions of NHE, VGLUT, and VMAT to these changes. Taken together, our findings suggest that DA SVs dynamically modulate their content through changes in pH. During periods of heightened neuronal activity, increases in pH drive further DA loading into SVs prior to fusion, thereby maximizing DA release. Such a mechanism may ultimately shed light on how subsets of actively firing DA neurons rapidly tune DA vesicle content to meet increased synaptic demand.

STAR★METHODS

Detailed methods are provided in the online version of this paper and include the following:

- KEY RESOURCES TABLE

- CONTACT FOR REAGENT AND RESOURCE SHARING

- EXPERIMENTAL MODEL AND SUBJECT DETAILS
  - *Drosophila* Rearing and Stocks
  - Mouse Strains and Animal Care

- METHOD DETAILS
  - *Drosophila* Brain Imaging
  - *Drosophila* Immunohistochemistry
  - Quantitative RT-PCR
  - *Drosophila* Electrophysiology

> – *Drosophila* Behavior
>
> – Mouse Brain Experiments
>
> – Electrochemical Recordings d
>
> • QUANTIFICATION AND STATISTICAL ANALYSIS

CONTACT FOR REAGENT AND RESOURCE SHARING

Further information and requests for resources and reagents should be directed to and will be fulfilled by the Lead Contact, Dr. Zachary Freyberg (freyberg@pitt.edu).

EXPERIMENTAL MODEL AND SUBJECT DETAILS

***Drosophila* Rearing and Stocks—**All *Drosophila melanogaster* strains were grown and maintained on standard cornmeal-molasses media at 25°C under a 12:12 h light-dark schedule. Fly stocks include the wildtype strain, $w^{1118}CS_{10}$ (wCS10), which is w^{1118} outcrossed into Canton-S for 10 generations. The following previously described transgenic stocks were also used: *UAS-dVMAT* (corresponding to the neuron-specific dVMAT-A isoform), UAS-dVGLUT, UAS-TeTxLC, *UAS-ArcLight* (a gift of Dr. M. Nitabach, Yale University, New Haven, CT), *UAS-dVMAT-pHluorin, UAS-mCD8::GFP* and *LexOp-6x mCherry*. Expression driver lines include *TH-GAL4* (a gift of Dr. S. Birman, Universite Aix-Marseille II-III, Marseille, France) - for expression in presynaptic DA neurons (Friggi-Grelin et al., 2003), *VGLUT-LexA* – for expression in neurons expressing dVGLUT (Baek et al., 2013), *daughterless-GAL4 (da-GAL4)* – for expression in most tissues, as well as *OK6-GAL4* and *D42-GAL4* – for expression in motor neurons. To ascertain changes in the intraluminal pH of DA synaptic vesicles in presynaptic DA terminals, *UAS-dVMAT-pHluorin* was genetically recombined with *TH-GAL4* on chromosome III. Fly RNAi strains include: UAS-VGLUT-RNAi (*UAS-Vglut-RNAi^HMS*, HMS02011, VALIUM20, target 3077–3098 nt), *UAS-GFP-RNAi* (obtained from Bloomington Drosophila Stock Center), and *UAS-mCherry RNAi* (obtained from Bloomington Drosophila Stock Center). We also used *dVMAT^P1*, a previously described *dVMAT* null mutant allele (Vmat^SH0459). Fly strains including the *UAS-dVMAT* and *UAS-VGLUT* transgenes as well as the *dVMATP^P1* allele were also outcrossed for 10 generations into the wCS10 wildtype genetic background.

Mouse Strains and Animal Care—All mice were housed in humidity-and temperature-controlled colony rooms maintained on a 12:12 h light:dark cycle with lights on at 07:00 hours. We used both wildtype C57BL/6J and homozygous floxed VGLUT2 mice (VGLUT2^flox/flox) on a C57BL/6J background (Slc 17 a6^tm1Lowl/J; The Jackson Laboratory strain 12898, The Jackson Laboratory, Bar Harbor, ME). All procedures were approved by the institutional review board and ethics committees of Columbia University and the New York State Psychiatric Institute, which are fully accredited by the Association for Assessment and Accreditation of Laboratory Animal Care (AAALAC) International. Animals were cared for in accordance with all appropriate animal care guidelines according to the National Institutes of Health Animal Care and Use Program as well as the Animal Research: Reporting of *In Vivo* Experiments (ARRIVE) guidelines for reporting animal research. Moreover, all efforts were made to ameliorate animal suffering.

METHOD DETAILS

Drosophila Brain Imaging

Drug Treatments: All drugs were diluted in adult hemolymph-like saline (AHL; 108 mM NaCl, 5 mM KCl, 2 mM $CaCl_2$, 8.2 mM $MgCl_2$, 1 mM NaH_2PO_4, 10 mM sucrose, 5 mM trehalose, 5 mM HEPES, 4 mM $NaHCO_3$; pH 7.5, 265 mOsm) as described earlier (Freyberg et al., 2016). Drugs were primarily applied by bath superfusion into a flow chamber at room temperature (25°C). In some experiments, drug was applied by air pressure ejection (0.1–5 s duration) onto brains submerged in AHL. In these pressure ejection experiments, drug was delivered to a pulled glass pipet directed at the MB-MV1 region at a distance of ~10 μm away from the brain using a Picospritzer II (Parker Hannifin Corporation, Cleveland, OH) pressure ejection system. To induce synaptic vesicle exocytosis or alkalization, we treated brains with KCl (40 mM), or CQ (100 μM) solutions, respectively, in AHL adjusted for ionic osmolarity). In experiments measuring contributions of Cl^- to depolarization-induced SV acidification, brains were treated with a modified form of AHL where 50% of the Cl^- was substituted with gluconate and accordingly adjusted to maintain ionic osmolarity. In experiments where NHEs were inhibited by the NHE blocker EIPA, brains were pretreated with EIPA (50 μM, 25°C) for 15 min followed by continued EIPA superfusion in AHL during imaging. In experiments with VGLUT inhibitor RB, brains were pretreated with RB (500 nM, 25°C) for 20 min followed by continued RB superfusion in AHL during imaging. In experiments measuring FFN206 destaining, the brains were loaded to steady state with 300 nM FFN206 (30 min, 25°C) and then treated with drug solutions also containing 300 nM FFN206 as described previously (Freyberg et al., 2016).

Imaging: An isolated, *ex vivo* whole adult fly brain preparation was obtained by rapid removal and microdissection of the brain from decapitated flies. This whole brain preparation was placed in a recording chamber (JG-23, Warner Instruments, Hamden, CT) for rapid drug application and exchange. Brain preparations were imaged under continuous flow on an Ultima multiphoton laser scanning microscope (Bruker Corporation, Billerica, MA) using a 20× (1.0 NA) water immersion objective lens (Carl Zeiss Microscopy LLC, Thornwood, NY). The illumination source was a Coherent Chameleon Vision II Ti: Sapphire laser (Coherent, Inc., Santa Clara, CA) and we typically used <5 mW mean power at the sample. To establish a baseline of fluorescent signal from the respective fluorescent probe prior to drug treatment, fluorescence was measured for a 10-min period (25°C) before drug application. Fluorescent emission was collected using a 460/50 nm FWHM bandpass emission filter for FFN206 (λ_{ex} = 820nm) and 525/50 nm FWHM bandpass filter for dVMAT-pHluorin (λ_{ex} = 920nm). Data acquisition was performed with Prairie View software (version 4.0.29, Bruker Corporation).

Image Processing and Analysis: For experiments involving FFN206 or VMAT-pHluorin imaging, maximum-intensity z-projections or single slice time series, respectively, were generated and quantified using the Fiji/ImageJ image-processing package (National Institutes of Health, Bethesda, MD). Unless indicated otherwise, all images were corrected for background fluorescence. A custom program written in MATLAB (version R2015a, Mathworks, Natick, MA) was used to smooth data using a moving average in order to quantify maximum/minimum fluorescence intensity changes. This program also compiled

raw data across different animals by: (1) interpolating data to better fit 250ms time intervals given inter-experimental variability in the frame acquisition times, (2) temporally aligning data by time of KCl onset given variability in drug superfusion, and (3) normalized changes in fluorescence (ΔF) to the initial fluorescence intensity ($F_{initial}$ or F_i), which was calculated as F_{final} - $F_{initial}$, where $F_{initial}$ was defined as pre-treatment MB-MV1 fluorescence. Change in single-plane FFN206 fluorescence ($\Delta F = F - F_{final}$) was normalized to baseline fluorescence after steady-state loading with FFN206 (F_i). Absolute peak values for FFN206 fluorescence were defined as values $\geq$ 2.5 standard deviations above the mean pre-treatment fluorescence baseline in MB-MV1 region. Relative peak fluorescence is defined as $(F-F_i)/F_i$. Decay half-times ($t_{1/2}$) were estimated using the least-squares method to fit fluorescence values to a single-exponential function preceded by a plateau phase: $F/F_i(t) = (F_i\text{-Plateau}) e^{[-(t-t_0)/\tau_{decay}]} + \text{Plateau}$ where $t_{1/2} = \tau_{decay} \ln2$ and where $F/F_i(t)$ is the normalized fluorescence value as a function of time. To quantify the half-life (decay-time of acidification; $t_{1/2}$) for dVMAT-pHluorin, data were fit to the following equation: $t_{1/2} = y_0 e^{-k(x-x_0)}$, where x_0 is the time at which the acidification begins. The time to peak takes into account both the x_0 and the half-life, and therefore accounts for parameters including diffusion. All raw data were graphed using the GraphPad Prism software package (GraphPad Software Inc., San Diego, CA).

***Drosophila* Immunohistochemistry—**Brains from adult male flies were dissected in either cold 1× phosphate-buffered saline (PBS) + 0.2% Triton-X (0.2% PBST) or cold 1× PBS alone and fixed in either cold Bouin's solution (Sigma-Aldrich) (5 min, 25°C) or in 4% paraformaldehyde (30 min, 25°C). Samples were washed multiple times in either 1× PBS or PBT (PBS + 0.1% Triton) and blocked in either 0.2% PBST + 5% NGS or PBT + 0.2% BSA + 2% normal goat serum (NGS) (1 h, 25°C). Brains were subsequently incubated either one or two nights at 4°C in primary antibody blocking solution followed by an additional one or two nights at 4°C for secondary antibody incubation. The following primary antibodies were used: rabbit anti-dVGLUT (1:10,000, a gift of Dr. A. DiAntonio, Washington University, St. Louis, MO), mouse anti-GFP (1:100, Thermo Fisher Scientific, Waltham, MA), mouse anti-Bruchpilot (nc82, 1:100; Developmental Studies Hybridoma Bank (DSHB) at the University of Iowa, Iowa City, IA), chicken anti-GFP (1:1,000; Abcam, Cambridge, MA) and rabbit anti-dsRed (1:500; Takara Bio USA, Inc., Mountain View, CA). The following secondary antibodies were used: donkey anti-mouse Alexa Fluor 488 (1:500, Thermo Fisher Scientific), donkey anti-rabbit Alexa Fluor 555 (1:500, Thermo Fisher Scientific), goat anti-mouse Alexa Fluor 647 (1:1,000; Thermo Fisher Scientific), goat anti-rabbit Alexa Fluor 555 (1:1,000; Thermo Fisher Scientific), and goat anti-chicken Alexa Fluor 488 (1:1,000; Thermo Fisher Scientific). After antibody labeling, brains were equilibrated in 70% glycerol in PBS and mounted in either Aqua-Poly/Mount (Polysciences, Inc., Warrington, PA) or VECTASHIELD Antifade Mounting Medium (Vector Laboratories, Burlingame, CA). Samples were imaged on a Zeiss LSM 5 confocal microscope using a 63× oil-immersion objective lens (Carl Zeiss Microscopy LLC) and images were acquired at 512×512 or 1024×1024 pixel resolution. The relative percentage of nerve individual terminals that were both VMAT- and VGLUT-positive was quantified by first counting the total number of VMAT-positive terminals labeled by the anti-GFP antibody, followed by the number of terminals that also shared anti-VGLUT antibody labeling. Results were expressed as the

percentage of terminals sharing this overlap ± SEM; results were based on quantitation of terminals from 7 individual adult fly brains. The average co-localization within dense clusters of DA terminals including MB-MV1 was calculated using the Fiji/ImageJ plugin, Colocalization Threshold. Colocalization between VMAT(+) and VGLUT(+) signals within these dense clusters of terminals was calculated using Pearson's correlation coefficient.

Quantitative RT-PCR—Total RNA from 20 heads of 10-day old adult *Drosophila* males was purified using TRIzol reagent (Thermo Fisher Scientific) and then treated with Ambion DNase I (RNase-free).

(Thermo Fisher Scientific) to remove DNA contamination. First-strand cDNA was synthesized using oligo-dT primers and Super-Script III Reverse Transcriptase (Thermo Fisher Scientific) according to manufacturer instructions. Quantitative RT-PCR was performed using 100 ng cDNA, 250 nM primers and Power SYBR Green PCR Master Mix (Thermo Fisher Scientific) in a 20 μL reaction volume. All samples were run in triplicate for 3 independent runs using a Mastercycler ep RealPlex (Eppendorf, Hauppauge, NY) PCR system and normalized against an endogenous internal control *Drosophila melanogaster* ribosomal protein 49 (Rp49). The Delta-Delta-Ct [C(T)] method was used to analyze the data (see Table S1). The following primers were used:

Rp49 Forward: 5'-CATCCGCCCAGCATACAG-3'

Rp49 Reverse: 5'- CCATTTGTGCGACAGCTTAG-3'

dVGLUT Forward: 5'-GCACGGTCATGTGGTGATTTG-3'

dVGLUT Reverse: 5'-CCAGAAACGCCAGATACCATGG-3'

Primer designs for the Rp49 Forward and Rp49 Reverse primers were described earlier (Beck et al., 2012). Results from da-GAL4/ UAS-dVGLUT RNAi flies were normalized relative to a RNAi control [da-GAL4/UAS-GFP RNAi] to determine effects of dVGLUT RNAi-mediated knockdown on brain dVGLUT expression as shown in Table S1.

***Drosophila* Electrophysiology—**Intracellular recordings from muscle 6, segment A3 or A4 were performed. Briefly, third instar larvae were dissected and recordings carried out in HL3 saline at physiologically relevant Ca^{2+} conditions (1.5 mM Ca^{2+}). Data was only analyzed from recordings where the resting membrane potential was less than –55 mV Recordings were performed using an Axoclamp 2B amplifier (Molecular Devices, Sunnyvale CA). Data were low-pass filtered at 1 kHz, digitized, and recorded to disk using a Digidata 1322A interface (Molecular Devices, Sunnyvale CA). Amplitudes and frequency of mEPSPs were measured using the peak detection feature of the MiniAnalysis program (Synaptosoft, Inc. Decatur, GA).

***Drosophila* Behavior—**To measure the locomotor response to amphetamine, we used the TriKinetics *Drosophila* Activity Monitoring (DAM) system. Adult flies were entrained for 7 days in 12:12 h light:dark (LD) cycles at 25°C on standard cornmeal-molasses medium. Flies were then transferred individually to activity tubes containing food consisting of agar (1%) and sucrose (3%), delivered in water (vehicle) or amphetamine solution (5 mM or 10

mM). Flies were continuously monitored (also in LD) for movement using activity monitors (DAM5, Trikinetics). Activity was measured as the number of times a fly crossed the infrared beam (counts) per hour. Activity data from day 2 of monitoring were averaged, normalized, and plotted as counts/hour. Change in activity in response to drug treatment was reported as percent change in mean counts per hour. Asterisks indicate the statistical significance of the difference in activity of flies fed drug as compared to flies of the same genotype fed vehicle. We determined statistical significance using two-way ANOVAs and post-hoc t-tests (α=0.05).

Mouse Brain Experiments

Virus Injections: We used a serotype DJ, replication-incompetent, adeno-associated virus (AAV) to drive *cre*-mCherry expression under the control of the EF1a promoter (AAV-DJ-EF1a-mCherry-IRES-cre-WPRE) in ventral tegmental area (VTA) neurons. As a control, we used AAV-driven expression of mCherry alone under the control of the EF1a promotor (AAV-DJ-EF1a-mCherry). Both *cre*-mCherry (DJ-EF1a mCherry-IRES-cre-WPRE) and mCherry (DJ EF1a-mCherry) constructs were packaged in an AAV vector by the Stanford Gene Vector and Virus Core (Stanford University, Stanford, CA). Mice between 66 and 104 days old were anesthetized with ketamine (90 mg/kg) + xylazine (7 mg/kg) and 1 μl of either AAV-DJ EF1a–cre-mCherry or AAV-DJ EF1a-mCherry (titer 1.0×10^8 and 4.3×10^7 genome copies/ml, respectively) were injected bilaterally into the VTA (AP −3.4 mm, DV −4.5 mm, L ± 0.5 mm relative to bregma). The virus was injected through glass pipettes (PCR micropipettes, Drummond Scientific, Broomall, PA) pulled to a tip diameter of 20–40 μm, with timed solenoid-controlled pulses of compressed air. Pipettes were left in place for 3 min after the injection to reduce back flux along the injection track.

Brain Tissue Preparation and Immunohistochemistry: 4-weeks post-viral injection, C57BL/6J mice were decapitated and acute 300 μm thick coronal slices were cut using a vibrating microtome at 4°C. Brain slices used for imaging were kept in oxygenated (95% O_2, 5% CO_2) artificial cerebrospinal fluid (ACSF) containing (in mM): 125 NaCl, 2.5 KCl, 26 NaHCO$_3$, 0.3 KH$_2$PO$_4$, 2.4 CaCl$_2$, 1.3 MgSO$_4$, 0.8 NaH$_2$PO$_4$, 10 glucose (pH 7.2–7.4, 292–296 mOsm/L). Slices containing the VTA were immediately post-fixed in a 4% paraformaldehyde (in 0.1M phosphate buffer solution). Slices containing the nucleus accumbens (NAc) were first used for FFN102 imaging experiments and then post-fixed in a 4% paraformaldehyde (in PBS). 24 h post-fixation slices were transferred into a cryoprotectant solution (30% glycerol, 30% ethylene glycol in 0.1 M Tris HCl, pH 7.4) and kept at −20°C until processing. Immunofluorescence-based methods were used to examine *cre* and mCherry expression. Sections were washed in PBS and then transferred to a 0.1M glycine solution for 30 min to quench aldehydes. Sections were then washed in PBS, blocked with NGS for 2 h, and incubated overnight with mouse monoclonal anti-TH antibody (MAB318, 1:5,000; EMD Millipore, Billerica, MA) and either rabbit polyclonal anti-DsRed antibody (1:2,500; Takara Bio USA, Inc., #632496), which recognizes mCherry or rabbit polyclonal anti-Cre antibody (1:1,000, a gift of Dr. C. Kellendonk, Columbia University, New York, NY). The next day, sections were washed, and incubated with secondary antibodies: goat anti-rabbit Alexa Fluor 555 (1:200; Thermo Fisher Scientific, A-21428) for 2 h with and goat anti-mouse Alexa Fluor 488 (1:200; Thermo Fisher

Scientific, A-11001) for 45 min. After washing, sections were mounted on slides using Prolong Gold mounting medium (ThermoFisher Scientific) and kept at 4°C prior to imaging.

Confocal Image Analysis: A Fluoview FV1000 confocal scanning microscope (Olympus America Inc., Center Valley, PA) was used for all confocal imaging. Fluorescence images used to visualize *cre*/TH or mCherry/TH co-localization in the VTA around the injection area or in the NA in the approximate area where FFN102 imaging was done. In each location, confocal photomicrograph stacks of 4 images were taken (20× oil objective; optical zoom 1× and 1 μm z-step increments; 800×800 pixels image frames). After acquisition, confocal stacks were z-projected and linearly adjusted for contrast and brightness using the ImageJ64 software package (National Institutes of Health, Bethesda, MD).

FFN102 Imaging: Acute medioventral striatal mouse brain slices containing the NAc core were allowed to recover for 1 h in oxygenated ACSF before use at room temperature. Slices were incubated with FFN102 for 30 min and then transferred to an imaging chamber (QE-1, Warner Instruments, Hamden, CT) and held in place with a platinum wire and nylon custom-made holder (Wong et al., 2011). This chamber was superfused (1 mL/min) with oxygenated ACSF, and the FFN-loaded slice was allowed to wash for 15 min prior to imaging. Fluorescent structures were visualized at >25 μm depth in the slice using an Ultima multiphoton laser scanning microscope (Bruker Corporation, Billerica, MA) using a 60× (0.9 NA) water immersion objective lens. Structures were illuminated using an interlaced scanning pattern of two different laser sources set to measure the ratio between protonated ($\lambda_{ex} = 740$ nm) and deprotonated ($\lambda_{ex} = 690$ nm) FFN102 ($pK_a = 6.2$) (Rodriguez et al., 2013). The illumination source for 690 nm light was a Coherent Chameleon Vision II Ti: Sapphire laser (Coherent, Inc., Santa Clara, CA) and for 740 nm light was a Spectra-Physics Mai Tai DeepSee Ti: Sapphire laser (Spectra-Physics, Santa Clara, CA). Fluorescent emission was collected using a 460/50 nm FWHM bandpass emission filter for FFN102 (λ_{em} max = 450 nm). Images were collected from a 5 μm thick z-stack (1 μm per step) of a 12×12 μm^2 field of view at an 80×80 pixel resolution and an imaging rate of 1.7 s per stack using Prairie View software (version 4.0.29, Bruker Corporation). This volume was imaged over 6 min, during which ACSF with increased KCl (40 mM) was applied to the slice using the perfusion system starting at 150 s. For experiments using the NHE blocker, 5-(N-ethyl-N-isopropyl)amiloride (EIPA), a single z-plane of a larger field of view (100×100 pixel, 44×44 μm^2) was imaged at a slower imaging rate (3.2 s) to minimize potential photoactivation of the inhibitor caused by the 690 nm excitation source. Acute brain slices were pretreated with 25 mM EIPA for 2.5 min prior to imaging and then continuously exposed to the inhibitor throughout the imaging experiment. For these experimental conditions, KCl (40 mM) was applied to the slice 250 s after the start of imaging.

FFN102 Ratiometric Data Analysis: Z-stacks generated from 690 nm excitation (protonated-FFN102 excitation) were condensed using a maximum-intensity z-projection and then average fluorescence across the field of view was quantified using the Fiji/ImageJ image processing software package (National Institutes of Health, Bethesda, MD). This process was repeated for the z-stacks generated from 740 nm excitation (deprotonated-FFN102 excitation) and the ratio between the respective emission intensities was plotted for

each time point over the 6-min time course. These values plotted over time represented relative changes between the ratios of protonated and deprotonated FFN102 across the field of view. In each plot (Figures 7B, 7D, and 7F), the Y-axis was normalized to the maximal change in the 740 nm/690 nm emission ratio following onset of KCl-induced vesicular exocytosis ($F_{740/690}$ set to 1.0). For each fluorescent ratio trace, the first 60 time points generated a 2nd order polynomial to be used for normalization of the entire trace. Further, the maximum alkalization observed after KCl-induced depolarization from each trace was used to generate an average-maximum per day. Each trace from an individual day was then normalized to this maximum. The acidification effect that occurred as a consequence of KCl-induced depolarization was then measured as a fraction relative to this maximum alkalization. For each trace, the area under the curve between the time KCl reached the slice (175 s into the imaging time course) and when the average ratio became >0 (270 s) was measured using the GraphPad Prism software package. The largest acidification area for each trace was then collected and compared between conditions using an unpaired two-tailed t-test for statistical significance. Data was presented as mean averages ± SEM from at least 3 different animals per condition and at least 2 slices per animal.

Electrochemical Recordings—Fast-scan cyclic voltammetry recordings were performed with 5 μm cylinder carbon fiber electrodes placed in acute striatal brain slices containing the NAc core. Acutely isolated slices were incubated in oxygenated ACSF (95% O_2/5% CO_2) at room temperature for 1.5 h and transferred to a recording chamber with perfused ACSF at 34°C. Electrical stimuli were delivered to the slice through a bipolar tungsten electrode. A carbon fiber recording electrode was placed at a distance of ?50–100 μm from the stimulating electrode. Brain slices were stimulated for three cycles; each cycle consisted of single pulses every 2-min followed by a train of stimulation (20 pulses, 20 Hz). Square pulses of 0.4-ms duration were produced by an ISO-Flex stimulus isolator triggered by a Master-8 pulse generator (A.M.P.I., Jerusalem, Israel). Stimulus magnitude was selected by plotting a current-response curve and selecting the minimum value that produced the maximum response. Triangular voltage ramps from a holding potential of −450 mV to +800 mV over 8.5 ms (scan rate of 295 mV/ms) were applied to the carbon fiber electrodes at 100-ms intervals. Current was recorded with an Axopatch 200B amplifier (Molecular Devices, Foster City, CA) filtered with a 10-kHz low-pass Bessel filter and digitized at 25 kHz (ITC-18 board, InstruTECH, Great Neck, NY). Triangular wave generation and data acquisition/analysis were controlled by custom-written computer routines in the IGOR Pro software package (WaveMetrics Inc., Lake Oswego, OR). Background-subtracted cyclic voltammograms obtained in DA solutions of known concentration were used to calibrate the electrodes and to identify released DA. We quantified the first derivative of the evoked responses to specifically distinguish newly released DA from basal extracellular DA as described previously (Walters et al., 2015). For comparison of single pulses between EIPA and ACSF vehicle-treated groups, evoked DA release after each pulse was normalized to the maximal DA release within each stimulation cycle. For trains of stimulation, EIPA or vehicle was applied following the second stimulation cycle. The amplitude of the response following a train of stimulation was normalized to the DA released by the SP preceding the train. Two-way repeated measures ANOVA was used for statistical analysis of the data.

QUANTIFICATION AND STATISTICAL ANALYSIS

Data acquisition and quantification were performed non-blinded. Data was acquired and imported into Microsoft Excel (Microsoft Corp., Redmond, WA). All statistical analyses for *Drosophila* experiments were performed in GraphPad Prism (version 7) and analyses for mouse experiments were performed in SPSS (version 24.0; IBM Corp., Armonk, NY). All data are presented as the mean ± SEM unless otherwise specified. Details including the exact value of n for each sample and *p* values are provided in each respective figure legend.

Statistical analyses were conducted using either unpaired t-tests (Figures 2C, 2D, 3B, 3D, 6B–6D, 7B, 7D, and 7E), one-way (Figures 5C and 5D), two-way (Figures 5E and 5F) or repeated measures ANOVAs (Figures 7H and 7I) as indicated in the respective figure legends. For one-way or two-way ANOVAs, follow-up Tukey's multiple comparisons tests were conducted. For repeated measures analyses, in the event of significant effects, follow-up paired sample t tests were performed (Figure 7I). All statistical comparisons were performed on data from 3 biologically independent replicates on separate experimental days. Significance was shown as $* = p < 0.05$, $** = p < 0.01$, $*** = p < 0.001$, $**** = p < 0.0001$ and not significant values were not noted or shown as NS.

Supplementary Material

Refer to Web version on PubMed Central for supplementary material.

Acknowledgments

References

Baek M, Enriquez J, Mann RS. Dual role for Hox genes and Hox co-factors in conferring leg motoneuron survival and identity in Drosophila. Development. 2013; 140:2027–2038. [PubMed: 23536569]

Barker DJ, Root DH, Zhang S, Morales M. Multiplexed neurochemical signaling by neurons of the ventral tegmental area. J. Chem. Neuroanat. 2016; 73:33–42. [PubMed: 26763116]

Beck ES, Gasque G, Imlach WL, Jiao W, Jiwon Choi B, Wu PS, Kraushar ML, McCabe BD. Regulation of Fasciclin II and synaptic terminal development by the splicing factor beag. J. Neurosci. 2012; 32:7058–7073. [PubMed: 22593074]

Birgner C, Nordenankar K, Lundblad M, Mendez JA, Smith C, le Greveés M, Galter D, Olson L, Fredriksson A, Trudeau LE, et al. VGLUT2 in dopamine neurons is required for psychostimulant-induced behavioral activation. Proc. Natl. Acad. Sci. USA. 2010; 107:389–394. [PubMed: 20018672]

Blakely RD, Edwards RH. Vesicular and plasma membrane transporters for neurotransmitters. Cold Spring Harb. Perspect. Biol. 2012; 4:4.

Boyd IA, Martin AR. The end-plate potential in mammalian muscle. J. Physiol. 1956; 132:74–91. [PubMed: 13320373]

Cao G, Platisa J, Pieribone VA, Raccuglia D, Kunst M, Nitabach MN. Genetically targeted optical electrophysiology in intact neural circuits. Cell. 2013; 154:904–913. [PubMed: 23932121]

Choi BJ, Imlach WL, Jiao W, Wolfram V, Wu Y, Grbic M, Cela C, Baines RA, Nitabach MN, McCabe BD. Miniature neurotransmission regulates Drosophila synaptic structural maturation. Neuron. 2014; 82:618–634. [PubMed: 24811381]

Chuhma N, Choi WY, Mingote S, Rayport S. Dopamine neuron glutamate cotransmission: frequency-dependent modulation in the mesoventromedial projection. Neuroscience. 2009; 164:1068–1083. [PubMed: 19729052]

Dal Bo G, Beérubeé-Carrieère N, Mendez JA, Leo D, Riad M, Descarries L, Leévesque D, Trudeau LE. Enhanced glutamatergic phenotype of mesencephalic dopamine neurons after neonatal 6-hydroxydopamine lesion. Neuroscience. 2008; 156:59–70. [PubMed: 18706980]

Daniels RW, Collins CA, Gelfand MV, Dant J, Brooks ES, Krantz DE, DiAntonio A. Increased expression of the Drosophila vesicular glutamate transporter leads to excess glutamate release and a compensatory decrease in quantal content. J. Neurosci. 2004; 24:10466–10474. [PubMed: 15548661]

Daniels RW, Collins CA, Chen K, Gelfand MV, Featherstone DE, DiAntonio A. A single vesicular glutamate transporter is sufficient to fill a synaptic vesicle. Neuron. 2006; 49:11–16. [PubMed: 16387635]

Eriksen J, Chang R, McGregor M, Silm K, Suzuki T, Edwards RH. Protons regulate vesicular glutamate transporters through an allosteric mechanism. Neuron. 2016; 90:768–780. [PubMed: 27133463]

Freyberg Z, Sonders MS, Aguilar JI, Hiranita T, Karam CS, Flores J, Pizzo AB, Zhang Y, Farino ZJ, Chen A, et al. Mechanisms of amphetamine action illuminated through optical monitoring of dopamine synaptic vesicles in Drosophila brain. Nat. Commun. 2016; 7:10652. [PubMed: 26879809]

Friggi-Grelin F, Coulom H, Meller M, Gomez D, Hirsh J, Birman S. Targeted gene expression in Drosophila dopaminergic cells using regulatory sequences from tyrosine hydroxylase. J. Neurobiol. 2003; 54:618–627. [PubMed: 12555273]

Goh GY, Huang H, Ullman J, Borre L, Hnasko TS, Trussell LO, Edwards RH. Presynaptic regulation of quantal size: K+/H+ exchange stimulates vesicular glutamate transport. Nat. Neurosci. 2011; 14:1285–1292. [PubMed: 21874016]

Grace AA, Bunney BS. The control of firing pattern in nigral dopamine neurons: burst firing. J. Neurosci. 1984; 4:2877–2890. [PubMed: 6150071]

Grygoruk A, Chen A, Martin CA, Lawal HO, Fei H, Gutierrez G, Biedermann T, Najibi R, Hadi R, Chouhan AK, et al. The redistribution of Drosophila vesicular monoamine transporter mutants from synaptic vesicles to large dense-core vesicles impairs amine-dependent behaviors. J. Neurosci. 2014; 34:6924–6937. [PubMed: 24828646]

Hnasko TS, Edwards RH. Neurotransmitter corelease: mechanism and physiological role. Annu. Rev. Physiol. 2012; 74:225–243. [PubMed: 22054239]

Hnasko TS, Chuhma N, Zhang H, Goh GY, Sulzer D, Palmiter RD, Rayport S, Edwards RH. Vesicular glutamate transport promotes dopamine storage and glutamate corelease in vivo. Neuron. 2010; 65:643–656. [PubMed: 20223200]

Hu G, Henke A, Karpowicz RJ Jr, Sonders MS, Farrimond F, Edwards R, Sulzer D, Sames D. New fluorescent substrate enables quantitative and high-throughput examination of vesicular monoamine transporter 2 (VMAT2). ACS Chem. Biol. 2013; 8:1947–1954. [PubMed: 23859623]

Morales M, Root DH. Glutamate neurons within the midbrain dopamine regions. Neuroscience. 2014; 282:60–68. [PubMed: 24875175]

Pereira DB, Sulzer D. Mechanisms of dopamine quantal size regulation. Front. Biosci. (Landmark Ed.). 2012; 17:2740–2767. [PubMed: 22652810]

Pizzo AB, Karam CS, Zhang Y, Yano H, Freyberg RJ, Karam DS, Freyberg Z, Yamamoto A, McCabe BD, Javitch JA. The membrane raft protein Flotillin-1 is essential in dopamine neurons for

amphetamine-induced behavior in Drosophila. Mol. Psychiatry. 2013; 18:824–833. [PubMed: 22710269]

Pothos EN, Mosharov E, Liu KP, Setlik W, Haburcak M, Baldini G, Gershon MD, Tamir H, Sulzer D. Stimulation-dependent regulation of the pH, volume and quantal size of bovine and rodent secretory vesicles. J. Physiol. 2002; 542:453–476. [PubMed: 12122145]

Preobraschenski J, Zander JF, Suzuki T, Ahnert-Hilger G, Jahn R. Vesicular glutamate transporters use flexible anion and cation binding sites for efficient accumulation of neurotransmitter. Neuron. 2014; 84:1287–1301. [PubMed: 25433636]

Rodriguez PC, Pereira DB, Borgkvist A, Wong MY, Barnard C, Sonders MS, Zhang H, Sames D, Sulzer D. Fluorescent dopamine tracer resolves individual dopaminergic synapses and their activity in the brain. Proc. Natl. Acad. Sci. USA. 2013; 110:870–875. [PubMed: 23277566]

Rossano AJ, Kato A, Minard KI, Romero MF, Macleod GT. Na(+)/H(+) exchange via the Drosophila vesicular glutamate transporter mediates activity-induced acid efflux from presynaptic terminals. J. Physiol. 2017; 595:805–824. [PubMed: 27641622]

Schenck S, Wojcik SM, Brose N, Takamori S. A chloride conductance in VGLUT1 underlies maximal glutamate loading into synaptic vesicles. Nat. Neurosci. 2009; 12:156–162. [PubMed: 19169251]

Sulzer D. How addictive drugs disrupt presynaptic dopamine neurotransmission. Neuron. 2011; 69:628–649. [PubMed: 21338876]

Takamori S. Presynaptic molecular determinants of quantal size. Front. Synaptic Neurosci. 2016a; 8:2. [PubMed: 26903855]

Takamori S. Vesicular glutamate transporters as anion channels? Pflugers Arch. 2016b; 468:513–518. [PubMed: 26577586]

Tamir H, Piscopo I, Liu KP, Hsiung SC, Adlersberg M, Nicolaides M, al-Awqati Q, Nunez EA, Gershon MD. Secretogogue-induced gating of chloride channels in the secretory vesicles of parafollicular cells. Endocrinology. 1994; 135:2045–2057. [PubMed: 7525261]

Tong Q, Ye C, McCrimmon RJ, Dhillon H, Choi B, Kramer MD, Yu J, Yang Z, Christiansen LM, Lee CE, et al. Synaptic glutamate release by ventromedial hypothalamic neurons is part of the neurocircuitry that prevents hypoglycemia. Cell Metab. 2007; 5:383–393. [PubMed: 17488640]

Walters SH, Robbins EM, Michael AC. Modeling the kinetic diversity of dopamine in the dorsal striatum. ACS Chem. Neurosci. 2015; 6:1468–1475. [PubMed: 26083009]

Wong MY, Sulzer D, Bamford NS. Imaging presynaptic exocytosis in corticostriatal slices. Methods Mol. Biol. 2011; 793:363–376. [PubMed: 21913113]

Zhang S, Qi J, Li X, Wang HL, Britt JP, Hoffman AF, Bonci A, Lupica CR, Morales M. Dopaminergic and glutamatergic microdomains in a subset of rodent mesoaccumbens axons. Nat. Neurosci. 2015; 18:386–392. [PubMed: 25664911]

Author Manuscript

Author Manuscript

Author Manuscript

Author Manuscript

Highlights

- Cell depolarization increases DA vesicular loading prior to release in flies

- Depolarization-induced SV hyperacidification drives increased DA vesicle loading

- VGLUT in DA SVs mediates depolarization-induced hyperacidification

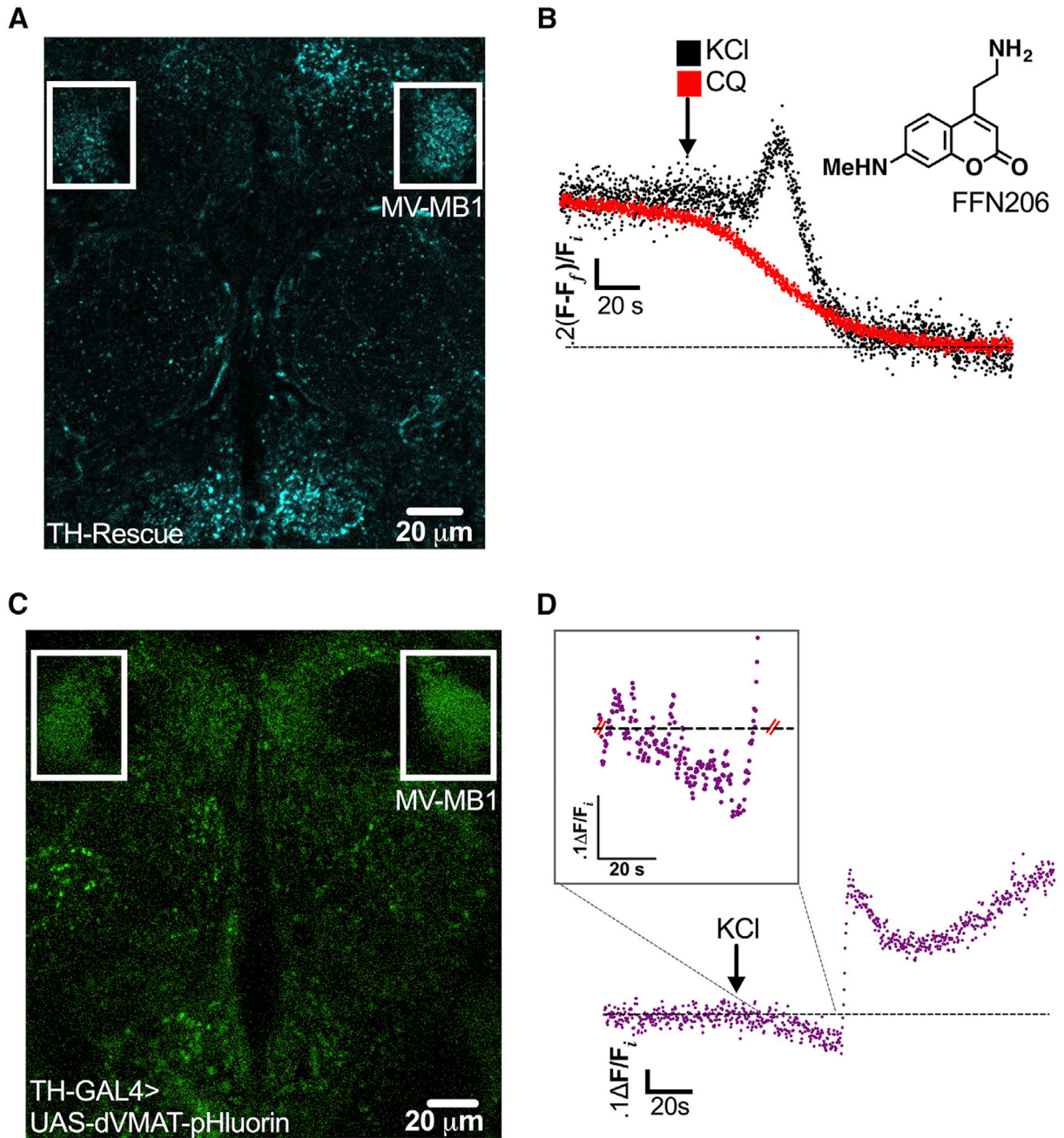- Depolarization-induced hyperacidification in DA SVs is conserved in mammals

Figure 1. Depolarization-Induced Increase in Vesicular Acidification Is Simultaneous with Increase in SV Filling in DA Terminals

(A) Presynaptic DA nerve terminals were labeled with FFN206 (300 nM, shown as a free base) in adult TH Rescue brains and subsequently treated with either KCl or CQ. The representative single-plane image highlights the MB-MV1 region (boxed in white; 25 μm scale bar; false color).

(B) An average of fluorescent imaging traces demonstrated a 21.5% ±3.4% increase in FFN206 vesicle filling prior to 40 mM KCl-induced destaining, best fit to a monoexponential decay (black trace, n = 4 flies). Weak base CQ (red trace, 100 μM) also

caused FFN206 destaining, best fit to a monoexponential decay ($t_{1/2}$ = 25.2 ± 2.6 s, n = 4), but with no additional vesicle filling prior to content release.

(C) dVMAT-pHluorin, a reporter of SV intraluminal pH, was expressed in DA neurons in a wild-type (WT) background (20 μm scale bar; false color). The representative single-plane image highlights MB-MV1 (boxed in white).

(D) Representative trace of dVMAT-pHluorin fluorescence measuring vesicular pH over time in response to KCl treatment (40 mM; arrow indicates treatment onset). KCl treatment induced a 14.7% ± 1.9% (n = 6) decrease in dVMAT-pHluorin fluorescence relative to the pre-KCl baseline, indicating a net increase in vesicle acidification. The trace displays changes in single-plane fluorescence intensity measured in ~250 ms intervals, corrected for background fluorescence, and normalized to initial values (F_i). Inset demonstrates a zoomed-in view of the period of KCl-induced vesicle acidification. All traces were recorded from the MB-MV1 region. Fly strains: WT background (*TH-GAL4, UAS-dVMAT-pHluorin*); TH Rescue (*dVMAT^P1^; TH-GAL4, UAS-dVMAT*).
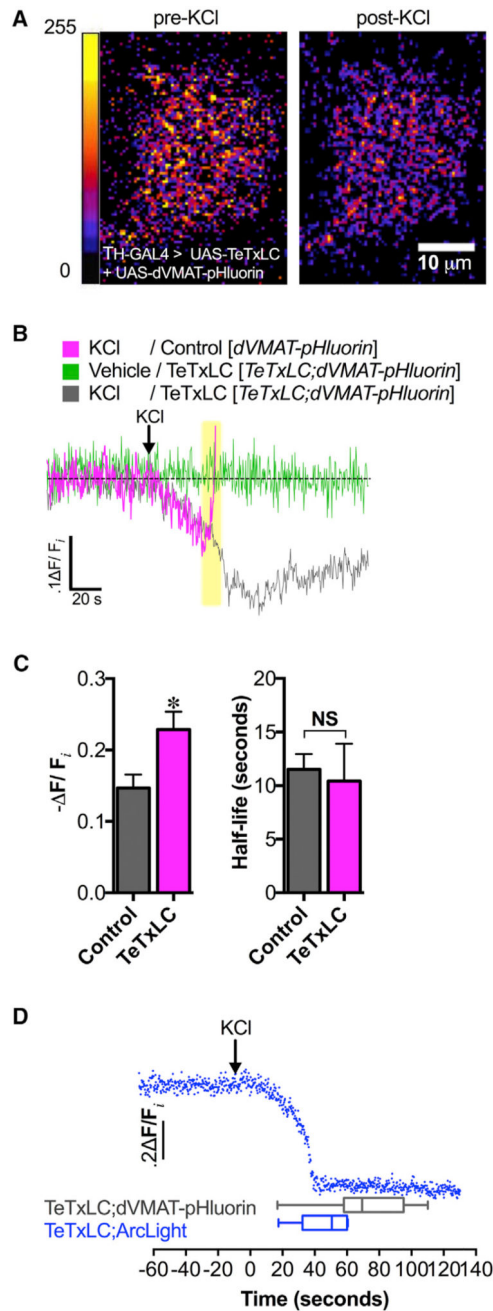
See also Figure S1.

Figure 2. Depolarization-Induced Increase in Vesicular Acidification Is Independent of Exocytosis

(A) High K$^+$ stimulation (40 mM KCl) caused increased SV acidification in DA nerve terminals as indicated by the decrease in dVMAT-pHluorin fluorescence (right) compared to pre-treatment (left) (10 μm scale bar; false color, arbitrary fluorescence intensity units). We show a representative single-plane image of DA nerve terminals in the MV-MB1 region in adult fly brains selectively expressing dVMAT-pHluorin and TeTxLC.

(B) Averaged dVMAT-pHluorin fluorescence traces measuring depolarization-induced changes in vesicular pH in TeTxLC-expressing DA terminals (gray trace) versus control DA terminals that do not express TeTxLC (magenta trace). DA terminal-selective expression of

TeTxLC eliminated the rapid dVMAT-pHluorin brightening associated with vesicle exocytosis in response to KCl (highlighted in yellow); vehicle treatment did not cause fluorescence changes (green trace).

(C) Expression of TeTxLC in DA terminals significantly enhanced SV acidification during KCl-induced stimulation relative to the pre-stimulation baseline (22.9% ± 2.5% decrease in dVMAT-pHluorin fluorescence, n=3 flies; gray bar) compared to controls where TeTxLC was not expressed (14.7% ± 1.9% decrease, n = 6; magenta bar) (p=0.037). TeTxLC expression did not affect the half-life to reach maximal acidification ($t_{1/2} = 10.4 \pm 3.5$ s, n = 3) compared to the non-TeTxLC control ($t_{1/2} = 11.5 \pm 1.4$ s, n = 6; p > 0.05).

(D) Optical recording of membrane depolarization of DA nerve terminals selectively co-expressing TeTxLC and ArcLight (top; blue trace). KCl treatment (indicated by arrow) decreased ArcLight fluorescence, indicating membrane depolarization. KCl-induced membrane depolarization (46.1 ± 6.7 s, n = 6) preceded exocytosis-independent vesicular acidification (71.9 ± 5.9 s, n = 17; p = 0.03). Error bars, SEM. Unpaired t tests were conducted for all analyses in (C) and (D). Fly strains: Control (*TH-GAL4, UAS-dVMAT-pHluorin*); TeTxLC background (*UAS-TeTxLC; TH-GAL4, UAS-dVMAT-pHluorin*); TeTxLC/Arc-Light (*UAS-TeTxLC; UAS-ArcLight/TH-GAL4*).
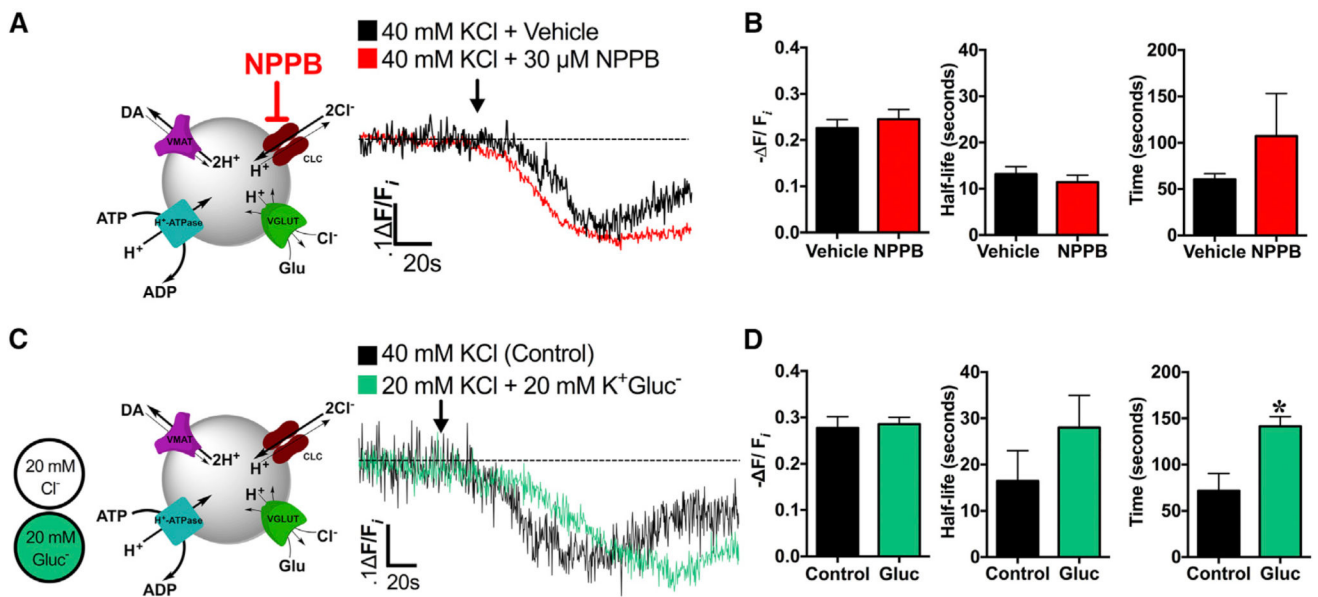
Figure 3. Depolarization-Induced Increases in SV Acidification Occur Independently of Acute Chloride Channel Inhibition or Diminished Extracellular Cl⁻

(A) Left: schematic illustrating ClC blockade by NPPB during high K^+ stimulation (40 mM KCl). Right: averaged dVMAT-pHluorin fluorescence traces measuring SV pH during high K^+ stimulation in brains acutely pre-treated with ClC blocker, NPPB (30 μM, 25°C, 15 min; red trace, n = 6 flies) compared to KCl stimulation alone (black trace, n = 3).

(B) NPPB pre-treatment (30 μM, 15 min, n = 6) did not significantly alter the time to reach maximal SV acidification (t = 107.3 ± 46.0 s), kinetics ($t_{1/2}$ = 11.4 ± 1.5 s), or magnitude of acidification during KCl stimulation ($-\Delta F/F_i$ = 24.5% ± 2.1%) compared to the non-NPPB pretreated control (t = 60.5 ± 6.0 s; $t_{1/2}$ = 13.2 ± 1.6 s; $-\Delta F/F_i$ = 22.6% ± 1.8%, n = 3; p > 0.05).

(C) Left: schematic illustrating isosmotic substitution of extracellular Cl⁻ with gluconate (GluCl⁻) during high K^+ stimulation (40 mM KCl). Right: averaged dVMAT-pHluorin fluorescence traces during stimulation under low Cl⁻ (20 mM Cl⁻, n = 5; green trace) or control conditions (40 mM Cl⁻, n = 3; black trace).

(D) Stimulation under low Cl⁻ (n = 5) did not significantly affect the kinetics ($t_{1/2}$ = 28.0 ± 6.0 s) or magnitude of depolarization-induced increases in DA vesicular acidification ($-\Delta F/F_i$ = 28.6% ± 1.5%) compared to control conditions (n = 3; $t_{1/2}$ = 16.4 ± 6.6 s, $-\Delta F/F_i$ = 27.7% ±2.4%; p > 0.05). Low Cl⁻ significantly delayed absolute time to maximal acidification (t = 141.4 ± 10.6 s) compared to control conditions (t = 71.7 ± 18.7 s; p = 0.01). An ~60 s baseline was recorded prior to KCl application (indicated by arrow). Error bars, SEM. Unpaired t tests were conducted for all analyses in (B) and (D). Fly strains: TeTxLC background (*UAS-TeTxLC; TH-GAL4, UAS-dVMAT-pHluorin*).
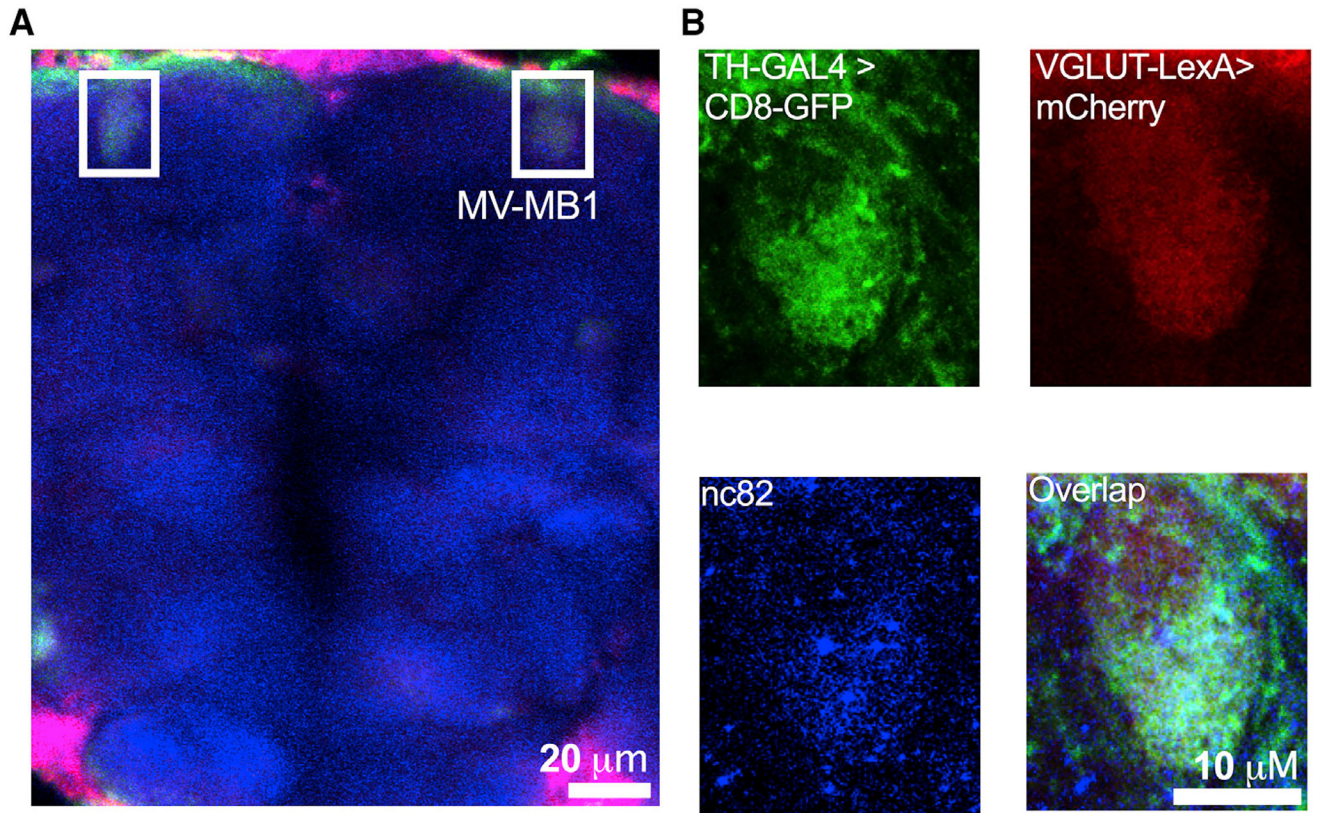
Figure 4. dVGLUT Localizes to Subpopulations of DA Nerve Terminals
Fluorescent tags were co-expressed by dVGLUT-LexA (mCherry) and TH-GAL4
(mCD8::GFP) enhancer-driven expression drivers in WT back-ground.

(A) Representative image from a projected z series highlights co-localization of dVGLUT-
and TH-promoter driven fluorescent tags in the DA terminal-rich MB-MV1 region (boxed in
white; 20 μm scale bar; false color).

(B) Single-channel images zoomed in on MV-MB1 show TH-GAL4-driven mCD8::GFP
(top left; green), VGLUT-LexA-driven mCherry (top right; red), and nc82 (labeling synaptic
active zone marker Bruchpilot; bottom left; blue). Merged image (bottom right) shows co-
localization of these fluorescent tags and nc82 labeling in DA terminal active zones. Fly
strain: *VGLUT-LexA/LexAOP-6x mCherry;TH-GAL4/UAS-mCD8::GFP*. Data are
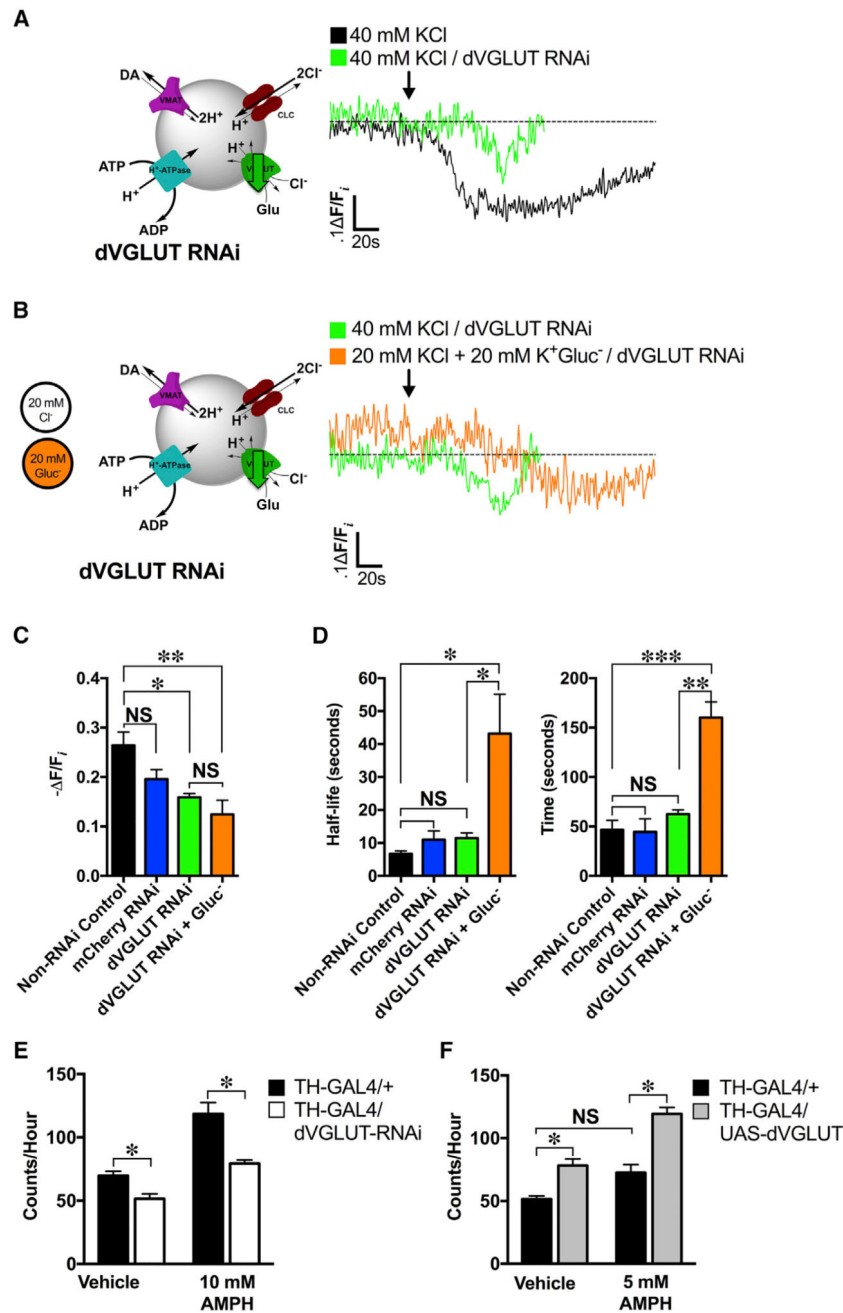representative of n > 3 experiments.

See also Figures S2 and S3.

Figure 5. VGLUT Mediates Depolarization-Induced SV Hyperacidification in DA Nerve Terminals and DA-Mediated Behavior

(A) Left: a schematic illustrating high K$^+$ stimulation (40 mM KCl) with concomitant dVGLUT RNAi knockdown. Right: representative dVMAT-pHluorin fluorescence traces showed decreased KCl-induced hyperacidification in the dVGLUT RNAi background (n = 3 flies; green trace) compared to the non-RNAi control (n = 4; black trace).

(B) Left: a schematic illustrating DA neuron stimulation (40 mM K$^+$) under low Cl$^-$ conditions by isosmotic gluconate (GluCl$^-$) substitution with concomitant dVGLUT RNAi knockdown. Right: representative dVMAT-pHluorin fluorescence traces comparing effects of low Cl$^-$ (orange trace; n = 3) to non-Cl$^-$ substituted controls (green trace; n = 3) on

depolarization-induced SV hyperacidification in a dVGLUT RNAi background in DA neurons.

(C) dVGLUT RNAi expression in DA neurons attenuated depolarization-induced increases in SV acidification ($-$ F/F$_i$ = 15.9% $\pm$ 0.7%; n = 3) relative to non-RNAi ($-$ F/F$_i$ = 26.4% $\pm$ 2.7%; n = 4) or mCherry RNAi ($-$ F/F$_i$ = 19.6% $\pm$ 1.9%; n = 5) controls (F$_{(3,11)}$ = 6.43, p = 0.009). Low Cl$^-$ (20 mM) conditions in a dVGLUT knockdown background did not further alter depolarization-induced increases in SV acidification ($-$ F/F$_i$ = 15.9% $\pm$ 0.7%; n = 3) compared to dVGLUT knockdown in unsubstituted (40 mM) Cl$^-$ conditions ($-$ F/F$_i$ = 12.4% $\pm$ 2.9%, n = 3; p > 0.05).

(D) dVGLUT RNAi knockdown did not significantly modify timing (t = 62.5 $\pm$ 4.4 s) or half-life (t$_{1/2}$ = 11.5 $\pm$ 1.6 s) to reach maximal acidification compared to the non-RNAi control (t = 46.6 $\pm$ 9.5 s; t$_{1/2}$ = 6.7 $\pm$ 1.0 s; p > 0.05) or mCherry RNAi (t = 44.5 $\pm$ 13.2; t$_{1/2}$ = 11.0 $\pm$ 2.7 s; p > 0.05) conditions. Low Cl$^-$ conditions significantly delayed the absolute time (t = 160.0 $\pm$ 16.0 s, n = 3; p = 0.002) and kinetics (t$_{1/2}$ = 43.2 $\pm$ 11.9 s, n = 3; p = 0.01) to reach maximal vesicle acidification compared to control levels of extracellular Cl$^-$ in the dVGLUT RNAi condition.

(E) RNAi knockdown of dVGLUT in presynaptic DA neurons (n = 27) diminished basal locomotion relative to that of control flies (26.2% reduction, n = 23; p = 0.0375). dVGLUT knockdown in DA neurons also decreased rates of hyperlocomotor activity in response to treatment with 10 mM AMPH compared to that of control flies (33.0% reduction, p < 0.0001; control: n = 16; dVGLUT RNAi: n = 68).

(F) dVGLUT overexpression in presynaptic DA neurons (n = 43) significantly increased basal locomotion under vehicle-fed conditions compared to control flies (52% increase, p = 0.0175; n = 23). Flies overexpressing dVGLUT in DA neurons exhibited greater rates of locomotion in response to AMPH than controls (64.4% increase, p < 0.0001; n = 23). This AMPH-induced hyperlocomotion was produced at an AMPH concentration (5 mM) otherwise insufficient to produce hyperlocomotion in control flies (p > 0.05). All experiments were conducted on 2 separate occasions.

(A)–(D): an ~60s baseline was recorded prior to KCl application (indicated by arrow). One-way ANOVAs with Tukey's multiple comparisons test: (C) and (D); two-way ANOVAs with Tukey's multiple comparisons test: (E) and (F). Error bars, SEM. Fly strains: dVGLUT RNAi (*UAS-TeTxLC; TH-GAL4, UAS-dVMAT-pHluorin/ UAS-dVGLUT RNAi*); non-RNAi control (*UAS-TeTxLC; TH-GAL4, UAS-dVMAT-pHluorin/+*); mCherry RNAi control (*UAS-TeTxLC/UAS-mCherry RNAi; TH-GAL4, UAS-dVMAT-pHluorin/UAS-TeTxLC*). Fly strains used in behavior: dVGLUT RNAi (*TH-GAL4/UAS-dVGLUT RNAi*); control (*TH-GAL4/+).* See also Figures S4–S6 and Table S1.
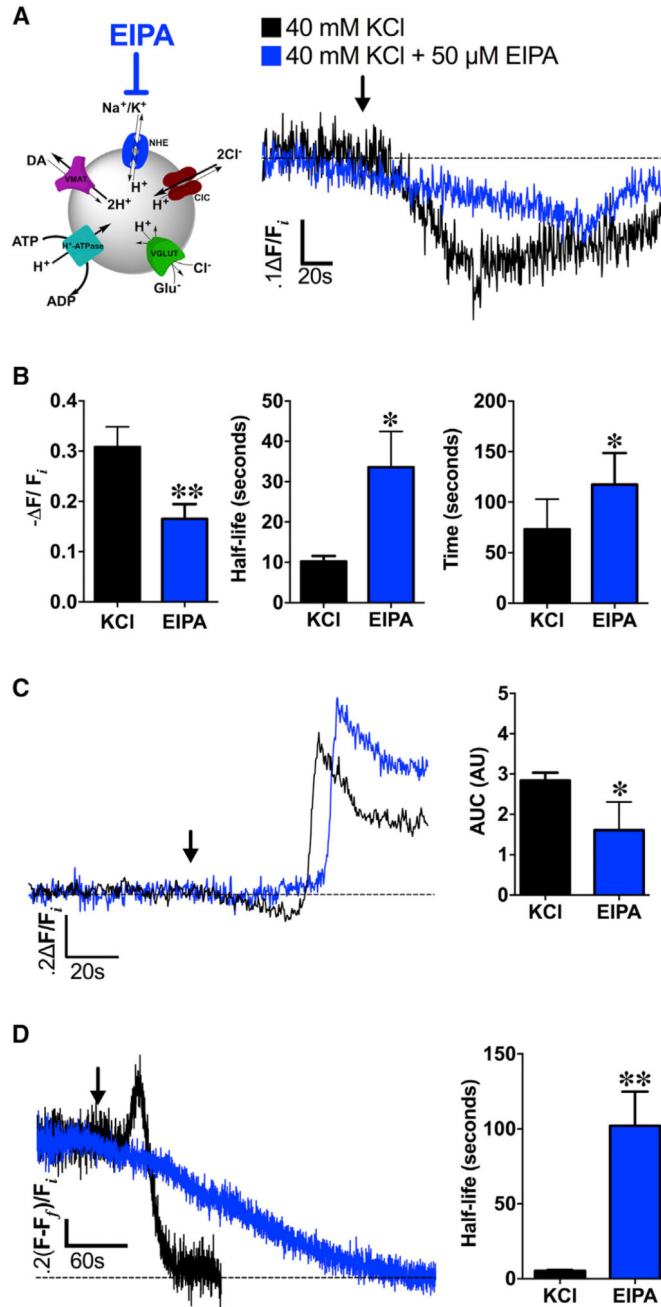
Figure 6. NHEs Mediate Depolarization-Induced Changes in SV pH and DA Content

(A) Left: schematic illustrating NHE inhibition by EIPA during high K^+ stimulation (40 mM KCl). Right: averaged dVMAT-pHluorin fluorescence traces measuring changes in SV pH during KCl stimulation in brains pre-treated with NHE inhibitor EIPA (50 μM, 15 min; blue trace, n = 5 flies) compared to high K^+ stimulation alone (black trace, n = 8).

(B) EIPA pre-treatment (n = 5) significantly decreased the magnitude of depolarization-induced SV hyperacidification compared to the non-EIPA control (n = 8; p = 0.02). EIPA pre-treatment also delayed the timing (t = 117.5 ± 14.0 s; p = 0.03) and kinetics ($t_{1/2}$ = 33.6

± 8.9 s; p = 0.004) to reach maximal vesicle acidification compared to the non-pretreated control.

(C) In the absence of TeTxLC expression in DA terminals, EIPA still attenuated SV hyperacidification preceding KCl-induced exocytic SV fusion (blue trace, n = 5) compared to the non-pretreated control (black trace, n = 6; p < 0.05); duration and magnitude of SV hyperacidification is represented as area under the curve (AUC). Curves represent average dVMAT-pHluorin fluorescence traces.

(D) Left: EIPA pre-treatment abolished depolarization-induced increases in DA vesicle loading in presynaptic DA nerve terminals (blue trace; n = 4) compared to non-pretreated controls (black trace; n = 4). Right: EIPA pre-treatment significantly slowed FFN206 vesicle destaining ($t_{1/2}$=102.1±22.8 s; n=4) compared to non-EIPA pre-treated controls ($t_{1/2}$ = 5.2 ± 0.9 s, n = 4; p = 0.005) as fit to a monoexponential decay.

An ~60 s baseline was recorded prior to KCl application (indicated by arrow). Unpaired t tests: (B)–(D). Error bars, SEM. Fly strains: (A) and (B): *TeTxLC; TH-GAL4, UAS-dVMAT-pHluorin;* (C): *+; TH-GAL4, UAS-dVMAT-pHluorin;* (D): *dVMAT^P1; TH-GAL4, UAS-dVMAT.*
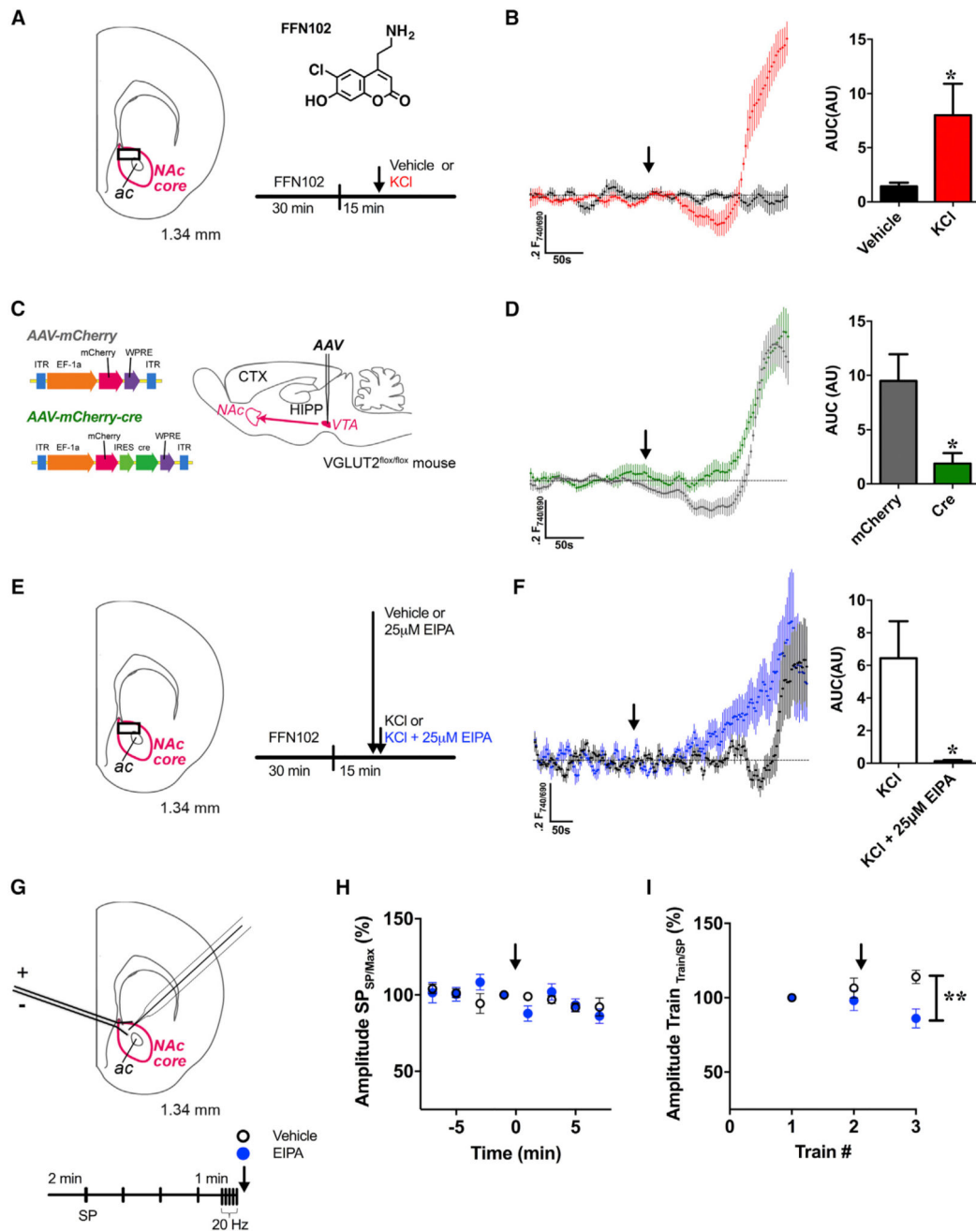
Figure 7. Depolarization-Induced SV Acidification Is Present in Mammalian DA Nerve Terminals and Mediated by VGLUT2 and NHE

(A) Schematic illustration shows the coronal brain slice used for FFN102 recordings through the NAc core (outlined in magenta). FFN102 imaging was conducted at the site indicated by the black box. The structural formula of FFN102 (phenol pK_a = 6.2, shown as a free base) is alongside the schedule for FFN102 release experiments. Medioventral acute brain slices were pre-loaded with FFN102 for 30 min followed by perfusion over a 15 min interval. Half the slices were perfused with ACSF (vehicle) and the other half with KCl (40 mM) after acquisition of an unstimulated baseline (indicated by arrow).

(B) Averaged traces of FFN102 fluorescence ratios in the presence (red trace) or absence (black trace) of KCl stimulation. KCl stimulation increased SV acidification ~6-fold relative to baseline (measured as AUC; n = 7 slices) compared to non-stimulated vehicle controls (n = 8; p = 0.03).

(C) Schematic of the constructs AAV-mCherry and AAV-mCherry-cre and an illustration of the VTA injection site for VGLUT2 cKO experiments.

(D) Averaged traces of FFN102 fluorescence ratios from mouse medioventral striatal brain slices in response to KCl stimulation. Slices were obtained from VGLUT2$^{flox/flox}$ mice injected with mCherry-tagged AAV-cre virus (VGLUT2 cKO, n = 6; green trace) or AAV-mCherry virus (control, n = 9; black trace). Experiments were conducted according to the schedule in (A). VGLUT2 cKO significantly reduced depolarization-induced SV hyperacidification compared to controls (p = 0.03).

(E) Schematic illustration of the coronal brain slice used for FFN102 recordings in EIPA experiments and alongside is the schedule. Brain slices from WT C57BL/6J mice were either pre-treated with EIPA (25 μM; 2.5 min) or ACSF vehicle, followed by KCl stimulation (40 mM; indicated by arrow) in the continued presence of EIPA or vehicle.

(F) Averaged traces of FFN102 fluorescence ratios in WT medioventral striatal brain slices acutely pre-treated with EIPA prior to KCl stimulation (blue trace) compared to vehicle pre-treated control slices (black trace). Acute EIPA treatment (n = 6) significantly decreased depolarization-induced hyperacidification prior to exocytosis compared with untreated controls (n = 7, p = 0.03); see STAR Methods for y axis normalization.

(G) Effects of electrical stimulation on striatal DA release paired with acute NHE inhibition. Schematic illustration shows the coronal brain slice used for FSCV recordings in the NAc core (outlined in magenta). Alongside is the schedule for electrical stimulation. Brain slices from WT mice were stimulated by single pulses (SPs; 1 ms, 40 μA) every 2 min followed by a train of stimulation (20 pulses, 20 Hz). This schedule was repeated three times with either EIPA (25 μM) or ACSF vehicle application following train 2.

(H) No significant differences in evoked DA release were detected between EIPA-treated (blue circle; n = 9) versus vehicle controls (open circle; n = 8) in response to SPs (p > 0.5). Evoked DA release after each SP was normalized to the maximal DA release within each stimulation cycle (arrow indicates onset of EIPA treatment).

(I) EIPA treatment (25 μM; blue circle, n = 9)decreased evoked DA release following the third train compared to the vehicle control (open circle, n = 8; p = 0.004). In vehicle-treated slices, a significant increase in evoked DA release was evident following repeated trains of stimulation (train 1 versus 3; p = 0.018). EIPA or the ACSF control was applied following the second stimulation cycle (indicated by arrow).

Unpaired t tests: (B), (D), and (E); repeated-measures ANOVAs: (H) and (I). Error bars, SEM: (B)–(D).
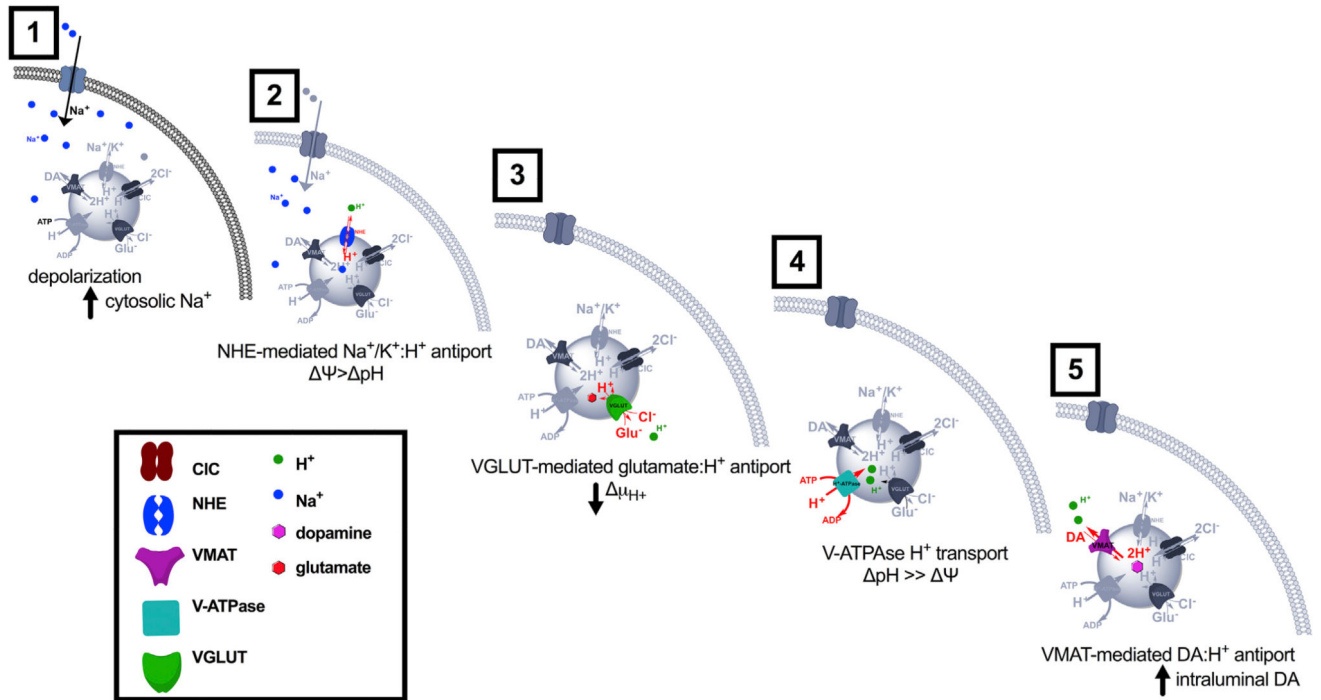
See also Figures S7 and S8.

Figure 8. Model for the Proposed Mechanism for Depolarization-Induced SV Hyperacidification
We propose a model for increases in SV acidification and content in DA terminals in response to neuronal stimulation as follows: (1) neuronal depolarization triggers increases in cytoplasmic Na^+ concentration; (2) NHE-mediated cation influx into SVs increases vesicle Ψ; (3) changes in Ψ drive glutamate transport into SVs via VGLUT; (4) the resulting buildup of intraluminal negative charge increases the vesicular proton-motive force, causing the V-ATPase to pump more H^+ into the vesicle; and (5) the rise in pH increases the driving force for VMAT-dependent DA loading into SVs.

KEY RESOURCES TABLE

REAGENT or RESOURCE	SOURCE	IDENTIFIER
Antibodies		
Rabbit anti-dVGLUT	DiAntonio lab	RRID: AB_2314347
Rabbit anti-Cre	Kellendonk lab	N/A
Mouse anti-*Drosophila* Bruchpilot (nc82)	Developmental Studies Hybridoma Bank (DSHB)	Cat# nc82; RRID: AB_528108
Mouse anti-TH	EMD Millipore	Cat# MAB318; RRID: AB_2201528
Mouse anti-GFP	Thermo Fisher Scientific	Cat# A-11120; RRID: AB_221568
Chicken anti-GFP	Abcam	Cat# ab13970; RRID: AB_300798
Rabbit anti-dsRed	Takara Bio USA	Cat# 632496; RRID: AB_10013483
Donkey anti-mouse Alexa 488	Thermo Fisher Scientific	Cat# A-21202; RRID: AB_141607
Goat anti-mouse Alexa 488	Thermo Fisher Scientific	Cat# A-11001; RRID: AB_2534069
Goat anti-chicken Alexa 488	Thermo Fisher Scientific	Cat# A-11039; RRID: AB_2534096
Goat anti-rabbit Alexa 555	Thermo Fisher Scientific	Cat# A-21428; RRID: AB_2535849
Donkey anti-rabbit Alexa 555	Thermo Fisher Scientific	Cat# A-31572; RRID: AB_162543
Goat anti-mouse Alexa 647	Thermo Fisher Scientific	Cat# A-21236; RRID: AB_2535805
Bacterial and Virus Strains		
AAV-DJ-EF1a-mCherry-IRES-cre-WPRE	Stanford University Neuroscience Gene Vector and Virus Core	GVVC# GVVC-AAV-84
AAV-DJ-EF1a-mCherry	Stanford University Neuroscience Gene Vector and Virus Core	GVVC# GVVC-AAV-97
Chemicals, Peptides, and Recombinant Proteins		
Aqua-Poly/Mount	Polysciences	Cat# 18606
VECTASHIELD	Vector Laboratories	Cat# H1000; RRID: AB_2336789
Bouin's solution	Sigma-Aldrich	Cat# HT10132
Paraformaldehyde	Sigma-Aldrich	Cat# P6148
TRIzol Reagent	Thermo Fisher Scientific	Cat# 15596026
Ambion DNase I (RNase-free)	Thermo Fisher Scientific	Cat# AM2222
SuperScript III Reverse Transcriptase	Thermo Fisher Scientific	Cat# 18080093
Power SYBR Green PCR Master Mix	Thermo Fisher Scientific	Cat# 4367659
D-Amphetamine hemisulfate (AM	Sigma-Aldrich	Cat# A5880
FFN206	Abcam; Hu et al., 2013	Cat# 144554
FFN102	Abcam; Rodriguez et al., 2013	Cat# 120866
5-(N-ethyl-N-isopropyl)amiloride (EIPA)	Sigma-Aldrich	Cat# A3085
Rose Bengal (RB)	Sigma-Aldrich	Cat# R4507
5-Nitro-2-(3-phenylpropylamino)benzoic acid (NPPB)	Sigma-Aldrich	Cat# N4779
Chloroquine (CQ)	Sigma-Aldrich	Cat# C6628
Magnesium D-gluconate hydrate	Sigma-Aldrich	Cat# G9130

REAGENT or RESOURCE	SOURCE	IDENTIFIER
Sodium gluconate	Sigma-Aldrich	Cat# S2054
Potassium gluconate	Sigma-Aldrich	Cat# P1847
Potassium chloride (KCl)	Sigma-Aldrich	Cat# P9333
Experimental Models: Organisms/Strains		
Drosophila: $w^{1118}CS_{10}$ (wCS10)	Krantz lab	N/A
Drosophila: *UAS-dVMAT*	Krantz lab	N/A
Drosophila: *UAS-dVGLUT*	DiAntonio lab; Daniels et al., 2004	N/A
Drosophila: *UAS-TeTxLC*	Bloomington *Drosophila* Stock Center (BDSC)	RRID: BDSC_28838
Drosophila: *UAS-ArcLight*	Nitabach lab	RRID: BDSC_51056
Drosophila: *UAS-dVMAT-pHluorin*	Krantz lab	N/A
Drosophila: *UAS-mCD8::GFP*	BDSC	RRID: BDSC_32184
Drosophila: *TH-GAL4*	Birman lab; Friggi-Grelin et al., 2003	N/A
Drosophila: *daughterless-GAL4* (*da-GAL4*)	BDSC	RRID: BDSC_55850
Drosophila: *LexAop-6x mCherry*	BDSC	RRID: BDSC_52271
Drosophila: *VGLUT-LexA*	Mann lab; Baek et al., 2013	N/A
Drosophila: *UAS-dVglut-RNAi^{HMS}*	BDSC	RRID: BDSC_40845
Drosophila: *UAS-GFP-RNAi*	BDSC	RRID: BDSC_9330
Drosophila: *UAS-mCherry RNAi*	BDSC	RRID: BDSC_35785
Drosophila: *dVMAT^{P1}*(Vmat^{SH0459})	BDSC	RRID: BDSC_29477
Drosophila: OK6-GAL4	BDSC	RRID: BDSC_64199
Drosophila: D42-GAL4	BDSC	RRID: BDSC_8816
Mouse: C57BL/6J	The Jackson Laboratory	Jax: 000664; RRID: IMSR_JAX:000664
Mouse: Slc17a6^{tm1Lowl}/J	The Jackson Laboratory	Jax: 012898; RRID: IMSR_JAX:012898
Oligonucleotides		
Rp49 Forward primer: 5'-CATCCGCCCAGCATACAG-3'	McCabe lab; Beck et al., 2012 (custom made by Thermo Fisher Scientific)	N/A
Rp49 Reverse primer: 5'-CCATTTGTGCGACAGCTTAG-3'	McCabe lab; Beck et al., 2012 (custom made by Thermo Fisher Scientific)	N/A
dVGLUT Forward primer: 5'-GCACGGTCATGTGGTGATTTG-3'	This paper (custom made by Thermo Fisher Scientific)	N/A
dVGLUT Reverse primer: 5'-CCAGAAACGCCAGATACCATGG-3'	This paper (custom made by Thermo Fisher Scientific)	N/A
Software and Algorithms		
MATLAB	MathWorks	https://www.mathworks.com/products/matlab.html RRID: SCR_001622
Fiji/ImageJ	National Institutes of Health (NIH)	https://imagej.net/Fiji RRID: SCR_002285

REAGENT or RESOURCE	SOURCE	IDENTIFIER
GraphPad Prism	GraphPad Software	https://www.graphpad.com/ RRID: SCR_002798
IGOR Pro	WaveMetrics	https://www.wavemetrics.com/products/igorpro/igorpro.htm RRID: SCR_000325
Excel	Microsoft	N/A
SPSS	IBM	http://www-03.ibm.com/software/products/en/spss-statistics/ RRID: SCR_002865